Master's thesis

2020

Hermann Brodin

NTNU
Norwegian University of
Science and Technology
Faculty of Engineering
Department of Marine Technology

Hermann Brodin

Hydrodynamic design of an affordable USV

Resistance prediction, design optimisation and VPP construction

June 2020

NTNU
Norwegian University of
Science and Technology

NTNU
Norwegian University of
Science and Technology

NTNU

Norwegian University of
Science and Technology

Hydrodynamic design of an affordable USV

Resistance prediction, design optimisation and VPP construction

Hermann Brodin

Submission date: June 2020
Supervisor: Luca Savio
Co-supervisor: Andreas Echtermeyer

Norwegian University of Science and Technology
Department of Marine Technology

Abstract

This report presents a study on the design of an affordable USV having 200kg displacement, and the investigation consist of four stages. The first stage is the development of a solver to predict the resistance of the vessel based on potential theory, empirical models, and a regression formula. Secondly, a particle swarm optimisation is carried out with respect to resistance. The third part involves CFD simulations of the vessel in various roll, trim, and yaw angles to obtain hydrodynamic load coefficients. Finally, a VPP is constructed based on the coefficients from CFD.

The resistance models for wave resistance in the first part is Michell's thin ship theory in combination with a regression formula for the wave resistance of a torpedo. The viscous resistance is predicted by the ITTC' 57 line and form factors proposed by MARINTEK and Hoerner. Large discrepancies between the resistance models and the CFD-results are observed, and the reason is expected to come from the deformation of the free surface not being accounted for by the resistance models.

In the second part is the optimisation of the geometry carried out six times at the vessel velocity 3m/s, and the five outputs with the lowest resistance are all in the interval from 132N to 134N. The two optimisation parameters with considerable variations are the torpedo size and the height of the keel, and the remaining five parameters are close to equal for all of the geometries.

In the third part is the best geometry obtained from the optimisation simulated in eight different orientations at 3m/s; two in roll, two in trim, three in yaw and one with no rotation. Additional three simulations are conducted in trim with zero vessel velocity to separate the static and dynamic loads.

In the fourth part is the loads from CFD made dimensionless by a set of coefficients. These coefficients are used to predict the hydrodynamic loads on the vessel at a given orientation and a given velocity by the VPP. For a specific wind speed and direction is the orientation and velocity of the vessel iterated until an equilibrium between sail loads and hydrodynamic loads are obtained.

According to the VPP is the vessel able to obtain a velocity of 2.5m/s if the vessel is beam reaching in 9m/s wind speed, which is the 50% percentile of the wind speed in the North sea. The VPP predict a velocity of the current vessel comparable to the successful SailDrone project, and somewhat faster than the smaller Sailbuoy.

The vessel is capable of resisting large roll moments but has possibilities for improvement in trim and yaw due to the length-to-breadth ratio being close to unity.

Sammendrag

Denne masteroppgaven presenter et arbeid som er gjennomført for å designe et rimelig priset ubemannet overflatefartøy. Oppgaven er delt inn i fire steg hvorav den første er å kombinere potensialteori, empiriske modeller og en regresjonsformel til en samlet motstandsmodell for å predikere motstanden til fartøyet. Det neste steget bruker motstandsmodellen til å gjennomføre en partikkelsvermeroptimalisering, for å minimere motstanden til fartøyet. Det tredje steget innebærer simuleringer med numerisk fluiddynamikk for å finne lastene som virker på fartøyet i konstant rull, stamp og gir. I det fjerde steget er lastene fra simuleringene brukt til å lage et hastighet prediksjonsprogram.

Bølgemotstandsmodellene i første steg er Michells tynt skip teori i kombinasjon med en regresjonsfunksjon for torpedoen. Den viskøse motstanden er predikert med ITTC 57' linjen og formfaktorene foreslått av MARINTEK og Hoerner. Det er observert store forskjeller mellom motstanden predikert av motstandsmodellene og resultatene fra simuleringene. Det er antatt at den største kilden til avvik kommer av at deformasjonen av den frie overflaten ikke blir tatt hensyn til av motstandsmodellene. I steg to er optimeringen gjennomført seks ganger med en hastighet på 3m/s, de fem optimeringene som endte med lavest motstand er alle innenfor intervallet 132N-134N. De to optimeringsparameterene med nevneverdig forskjell blant geometriene er størrelsen på torpedoen og høyden på kjølen. De resterende fem optimeringsparameterene er tilnærmet lik for alle geometriene.

I det tredje steget er den beste geometrien fra optimeringen simulert med en hastighet på 3m/s i åtte forskjellige orienteringer; to i rull, to i stamp, tre i gir og en rett frem. I tillegg er tre simuleringer i stamp gjennomført med null hastighet for å skille de dynamiske og statiske kreftene.

I det fjerde steget lastene fra simuleringene gjort dimmensjonsløse ved hjelp av koeffisienter. Disse koeffisientene blir brukt av hastighets prediksjonsprogrammet for å predikere hastigheten til fartøyet ved en gitt hastighet og orientering. Ved en spesifisert vindhastighet of vindretning blir orienteringen og hastigheten til båten iterert helt til en likevekt mellom seilkreftene og de hydrodynamiske kreftene er oppnådd.

Ifølge hastighets prediksjonsprogrammet er fartøyet i stand til å oppnå en hastighet på 2.5m/s med en sidevind på 9m/s, som er vindhastigheten ved 50% prosentilet i Nordsjøen. Hastigheten til fartøyet i dette studiet oppnår sammenlignbar hastighet som SailDrone prosjektet og er noe raskere enn det mindre fartøyet Sailbuoy.

Fartøyet har gode egenskaper for å motstå moment i rull, men har forbedringspotensialet i stamp og gir siden det er nesten like bredt som langt.

Preface

This report is written as the master thesis at the Norwegian University of Science and Technology(NTNU) and the Department of Marine Technology during the spring term in 2020. The thesis is a part of a greater project led by Andreas Echtermeyer at the Department of Engineering Design and Materials at NTNU.

The original plan for the thesis was to design a USV and conduct towing tests with varying roll, trim and yaw angles and with different position of the torpedo and keel. The outbreak of the COVID-19 virus restricted the use of the testing facilities, hence the towing test were cancelled. Therefore, the scope of the thesis was changed in the middle of March by substituting the towing tests with CFD-simulations, and additionally constructing of a VPP.

I would like to thank my supervisor Professor Luca Savio for excellent guidance and motivation. He has been generous with his time and contributed with great and constructive ideas, especially when the scope of the thesis was modified.

I would also like to thank my office colleagues for all the help and support, and the excellent work environment.

Hermann Brodin
Oslo, 27.06.2020

Table of Contents

Nomenclature

ΔC_F	Resistance due to surface roughness
η	y-coordinate of hull surface
$\mathbf{I}_{3/2}$	The modified Bessel function
$\mathbf{J}_{3/2}$	The Bessel function
∇	Displacement
ν	Kinematic viscosity
ϕ	Roll angle or constant in MARINTEKs formula
ψ	Yaw
ρ	Water density
θ	Trim angle or wave propagation direction
C_B	Block coefficient
C_R	Residual resistance coefficient
C_T	Total resistance coefficient
C_{AA}	Air resistance coefficient
C_{BDM}	Transom stern resistance coefficient
C_F	Frictional resistance coefficient
C_P	Prismatic coefficient

COB	Center of buoyancy
COG	Center of gravity
COP	Center of pressure
D	Torpedo diameter
Fn	Froude number
Fn_D	Depth Froude number
g	Gravitational acceleration
GZ	Righting arm
k	Form factor
L_{CB}	Longitudinal centre of buoyancy measured from mid-ship
Lpp	Length between perpendiculars
R_F	Frictional resistance
R_T	Total resistance
R_W	Wave resistance
Re	Reynolds number
S	Wet hull surface
T	Draught
U	Particle velocity in PSO
u_τ	Friction velocity
V	Vessel velocity
$y+$	Dimensionless wall distance

Chapter 1

Introduction

Our dependence on the oceans is immense. They produce more than 50% of the oxygen we breathe and store about 26% of the co2 we emit, according to Sabine et al. 2004. They distribute heat from the low latitude regions to the high latitude regions and control the weather patterns. We harness seafood from the oceans and use them for more than 80% of the world's transportation, IMO 2020. These are just a few examples of how important the oceans are for us, and it substantiates UNESCO's statement, "We depend on the ocean for our well-being, yet its importance is not matched by our knowledge" UNESCO 2020. The recent focus on global warming and climate change amplify the importance of broadening the knowledge of our oceans. If politicians and businesses get a more extensive basis to support their measures, they are more likely to find the correct measures at the right time.

The state of the art of ocean monitoring is by satellites, commercial ships, research vessels, and buoys. Satellites can measure ocean bathymetry, sea surface temperature, sea level, ocean colour, coral reefs, and sea ice, NOAA 2020. Commercial ships add up to a large fleet, but the shipping lanes are quite restricted in terms of geographical span and consequently the data obtained, Smith et al. 2019. The data collection from commercial vessels include weather reports and ocean observations, and some are equipped with a flow-through seawater system that measures sea temperature, salinity, plankton concentration, microplastic concentration, fluorescence transmissivity, and other biogeochemical properties. The drawbacks of commercial ships using flow-through systems are the disturbed inflow by the ship wake and the uncertainty related to the draught of the system. The fleet of research vessels is smaller in scale but is not restricted to follow the commercial shipping lanes. These vessels can measure the same properties as commercial ships with higher accuracy and additionally, the gradient of these properties in the water column. Weather buoys typically measure air and sea temperature, wave height, wave periods and wind speed.

The motivation of developing a remotely operated vessel is to monitor the ocean outside of the regular shipping lanes. There are numerous benefits by using small unmanned surface vessels (USVs) compared to the research vessels. Without any crew present, there is no personal risk involved, which facilitate operations even in the hazardous and non-friendly environment. Having a crew onshore that operates numerous vessels require less salary compared to having a crew on every single vessel. Additionally, by omitting accommodation and other functions that are intended to aid the crew, the manufacturing cost can be significantly reduced. These two reasons give the USV an economic upper hand compared to the research vessel. Vice versa with a fixed budget, will the low cost of a single USV permit a larger fleet and consequently a larger extent of the oceans to be monitored compared to a research vessel. The main drawbacks are the limited payload and low propulsive power. Limited payload restricts the amount of equipment and sensors, and limited propulsion introduces difficulties to overcome the added resistance caused by flow-through systems. The absence of crew means there are no personnel to fix defects that may occur to the propulsion system, equipment or structure and also resolve the situation if the vessel entangles in a ghost net or get stuck in sea ice.

There are some successfully USVs in the literature, which is further discussed in the literature review. However, these are somewhat expensive, and the curves of the hull shape require special tools to construct. This project, on the other hand, investigates the possibility to combine hull components of simple geometry to reduce the manufacturing cost. This thesis will, therefore, address a potential USV design optimised in terms of resistance and then establish its hydrodynamic performance.

The approach to the problem has been to settle on the general design. Then, a combination of different resistance models is combined to predict the total resistance of the vessel. A set of optimisation parameters and constraints are determined, and the vessels geometry is optimised with respect to resistance. The geometry obtained from the optimisation is subsequently evaluated in CFD-simulations at various angles in roll, trim and yaw and to find the load coefficients. The load coefficients are then used to construct a velocity prediction program(VPP) to identify its hydrodynamic abilities.

The thesis will first give a literature review where previous USVs and VPPs are examined. In the method, the geometry is described and justified, then the approach to predict the resistance is calculated. The method also describes how the optimisation is carried out, how the CFD simulations are conducted and finally, the construction of the VPP. In the validation chapter, it is tested that Michells Thin Ship theory is written correctly and that the PSO code works. Then it is reviewed whether the empirical methods and potential theory coincide with results from CFD. In the result chapter is the optimised geometry presented along with its resistance curve. Then the results from CFD is presented, followed by the results from the VPP.

The overall project is divided into the three separate master thesis; hydrodynamic performance, sail arrangement and construction. This thesis will only examine the hydrodynamic aspect of the problem. Thus the only restriction in terms of cost reduction is to keep the geometry simple. Therefore, this thesis does not cover the building- and material expenses or whether the budget is overspent or not.

Chapter 2

Literature Review

2.1 USV

Veers and Volker 2006 has provided a history of USVs from world war two until the publication in 2006, and is referred to in the two first paragraphs. In 1946, the American Navy introduced a USV to collect samples from the atomic bombs on Bikini Atoll. In the 50s they utilised a USV to perform mine sweeping and in the 60s as moving target drones for firing practice. New prototypes for both minesweeping and target drones kept on coming and is still applicable today. The following decades and the applicability extended to munition supply in the late 60s. From the 90s USVs were used as reconnaissance and surveillance drones. The Israeli Navy has developed a USV combat platform equipped with a machine gun to keep the personnel unexposed.

What the majority of the military USVs have in common, is the operating time is in the range of hours or a few days. Also, the displacement is heavy and usually in the order of tonnes, or the velocity is high and sometimes both. The result, either way, is a high demand for power. Due to the short operation time, high power requirement and precise manoeuvrability, they are generally running on fossil fuels.

One of the only sail powered USVs in the litterature is the Sailbouy project presented in Ghani et al. 2014. The vessel is 2m long and have a 60 kg displacement, which is smaller than the vessel considered in the present study. The Sailbouy completed a two month mission in the Gulf of Mexico covering a cumulative total distance of 2400km and a average vessel speed of 0.42m/s, with an average wind speed of 6m/s

The recent developments of cybernetics and the increased interest in environmental change have resulted in the development of commercial USVs for ocean monitoring. Companies such as Autonatut, Saildrone, and Open Ocean Robotics have developed commercial USVs for ocean monitoring, and the two latter has stated a mission duration of 12 months. They all use renewable energy for propulsion, specifically Autonaut harness en-

ergy from the waves while Saildrone and Open Ocean Robotics harness wind energy. They all have double curvature monohulls, and the resistance prediction is not available to the public.

2.2 VPP

A velocity prediction program is a computer program that balances the hydrodynamic forces acting on the hull with the aerodynamic forces acting on the sail. Obtaining the exact hydrodynamic forces is difficult since it depends on all the degrees of freedom and the coupling between them. The hydrodynamic forces are also dependent on the hull geometry, so if the program is designed for various hulls, generalisations of the force prediction are needed. The designer of the program decides how complex the VPP is, by how many degrees of freedom is considered, how the force is determined, whether unsteady effects are included etc.

Cairoli 2002 constructed a VPP for monohull sailing yachts where the resistance was decomposed into upright resistance, heeling resistance, induced drag, and added resistance in waves. Towing tests for two different vessel series and seven different geometries were carried out at different heeling angles, and the total resistance was measured. According to the author, the VPP suffered from limited experimental data and had trouble with determining the residuary resistance with heel angles.

Some commercial software exists such as WinDesign, AHVPP and Sailfish Yacht Analyzer. However, to the authors knowledge none of these are compatible with the geometry in the present study.

Chapter 3

Method

3.1 Geometry

It is stated in the introduction that the hull shape is constrained to a simple geometry to keep the cost low. Simple geometry in this context means surfaces curved in no more than one direction and bodies of revolution. Additionally, since the original plan was to conduct towing tests and the workshop that was supposed to construct the model had a busy schedule, keeping the geometry uncomplicated was a necessity.

The first geometry considered is a monohull with a sail and a keel similar to a regular sailboat. However, this configuration is already investigated by some of the projects mentioned in the literature review, and it was therefore suggested to investigate a different design.

The second geometry considered is a catamaran hull to get a larger deck area for solar panels and sensor equipment. Due to the short length of the vessel, it enters the region of Froude numbers where the wave resistance increases rapidly even at moderate speeds. A small water-plane area twin-hull(SWATH) was therefore considered due to its low wave-making resistance. The main problem with SWATH in this project is its insufficient righting moment in roll. That is a terrible characteristic when the vessel use sail for propulsion. The lateral forces from the sail will then induce a significant roll moment which exceeds the righting moment produced by the buoyancy.

A third and final configuration was therefore considered. This configuration consist of two displacement hulls referred to as side hulls and a middle section composed by a torpedo and a keel. The side hulls have a constant water-plane section described by equation (3.1). The same equation expresses the keel, but with different constants and without the last term.

$$y = \pm ax^2 + c \pm \frac{B_{vessel}}{2} \tag{3.1}$$

The constant c is equal to half of the side hull beam and a=-4cL_{pp}^2. The torpedo is a fusion of three sections, the front is a half dome, the middle body is a cylinder, and the stern is a cone. A visualisation of the geometry is presented in figure 3.1.

So far, it is indicated that the propulsion of the vessel is purely provided by sail. However, it is proposed that a propeller is installed at the rear end of the torpedo and generate propulsion when the wind is absent. A brushless DC motor will provide the power to the propeller at unsuitable sailing conditions and work as a generator when the sailing conditions are right. In this way, the vessel can obtain a more consistent velocity. To study the optimal design of the propeller and its effect on the hydrodynamics of the vessel would have been compelling. However, it is dedicated to further work to reduce the scope of this thesis.

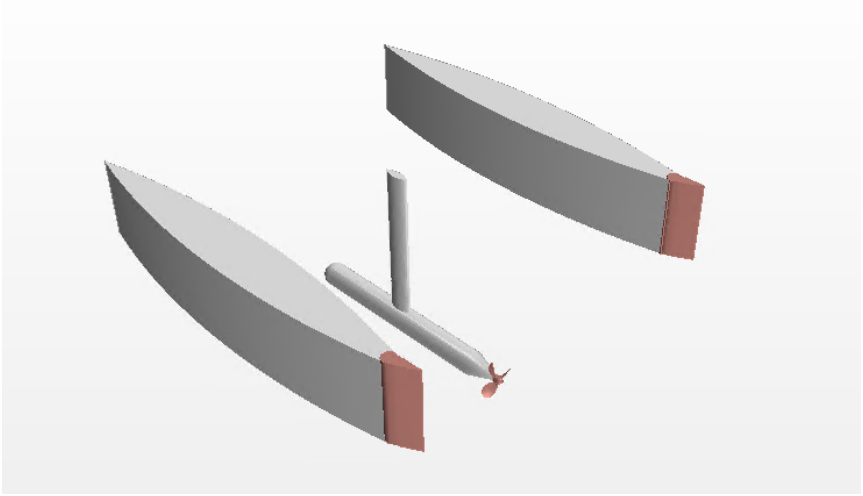

Figure 3.1: The USV design with rudders and propeller.

The concept of this geometry is that heavy equipment like batteries and propulsion system are placed in the torpedo, hence lowering the centre of gravity which has a positive effect on the stability. The submerged torpedo will also produce buoyancy significantly while the wave resistance is kept at a minimum. The keel is an excellent base for the sail mast and connects the torpedo to the side hulls. How the side hulls and the keel is structurally connected is not discussed in this thesis since it is irrelevant for the hydrodynamics.

It was considered to use a transom stern for the side hulls, rather than the pointy sterns in figure 3.2. This will be described later in this chapter. Instead of going for a transom stern, the side hulls will be fitted with a rudder that naturally follows the existing shape, as shown in figure 3.1. The propeller and the gap between the rudders and the side hulls are omitted in the resistance prediction due to simplicity reasons. Thus the geometry used in the rest of the thesis is presented in figure 3.2.

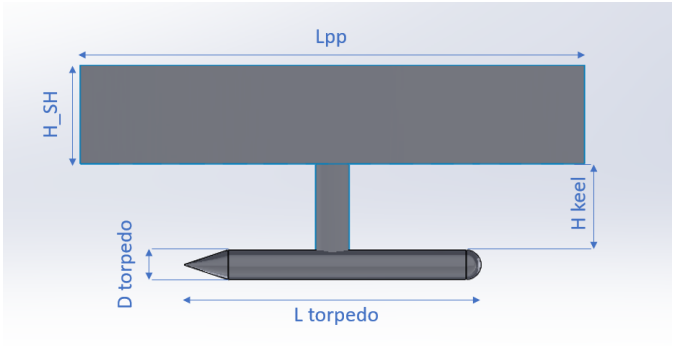

(a) Sideview

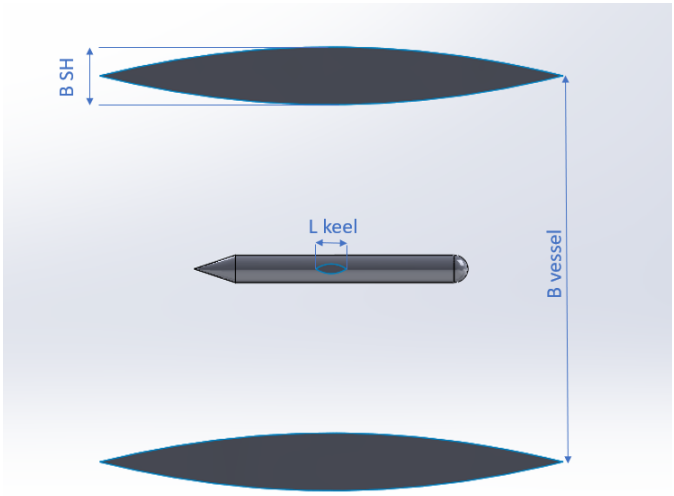

(b) Top view

Figure 3.2: Geometry and dimensions of the vessel.

3.2 Total Resistance

Due to the complexity of the flow surrounding the hull, it is currently no simple method to find the exact resistance of a vessel. However, there are methods that give reasonable estimations if the problem is decomposed into the separate physical phenomenons occurring. Each of these contribution are estimated by empirical formulas, experimental values or computer simulations. For convenience it is common to express the resistance components with coefficients, where the total resistance coefficient is given by

$$C_T = \frac{R_T}{0.5\rho V^2 S}, \tag{3.2}$$

where R_T is the total resistance, ρ is the density of the surrounding water, V is vessel velocity and S is the wet surface. The total resistance coefficient can be decomposed

according to equation (3.3).

$$C_T = (1 + k)(C_F + \Delta C_F) + C_R + C_{AA} + C_{BDM} \tag{3.3}$$

The first term in equation (3.3) account for the viscous resistance with k being the form factor, C_F the frictional resistance coefficient and ΔC_F the roughness coefficient. C_R is the residual resistance coefficient, C_{AA} is the air resistance and C_{BDM} is the base drag resistance.

Both C_F and C_R can be decomposed further according to figure 3.3. The three approximately horizontal lines in figure 3.3 form the contributions to the viscous resistance, while the strictly increasing lines contribute to the residual resistance.

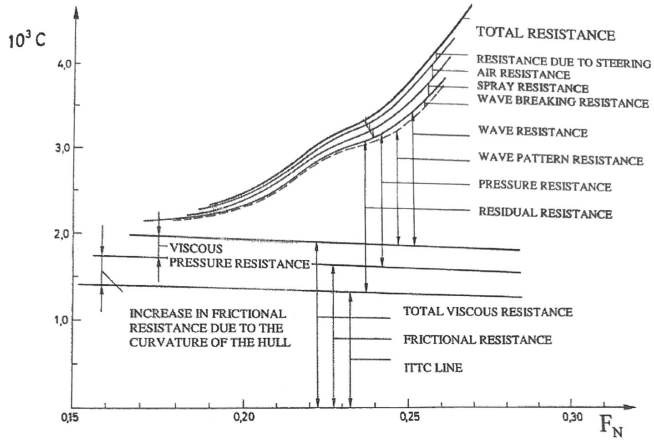

Figure 3.3: Resistance components of a typical displacement ship Harvald 1983 (sjekk referansen)

To optimise the vessel geometry with respect to resistance, it is necessary to determine the resistance coeficients efficiently, i.e. $\mathcal{O}(seconds)$ or $\mathcal{O}(minutes)$. Model tests and CFD simulations are too time consuming and expensive to be appropriate for this problem.The roughness resistance, can according to Steen 2014 be excluded for Re below 10^8 hence ΔC_F is neglected in this project. The optimisation of the vessel geometry is therefore based on empirical models and potential theory. The resistance related to steering, air resistance, spray resistance and wave breaking resistance is neglected in the optimisation method due to two reasons. Firstly, the contributions from these components are small compared to the viscous resistance and the wave resistance. Secondly, except for the air resistance, they introduce far more complexity to the problem. The specific models used to determine the resistance components for the optimisation are given in table 3.1.

Table 3.1: Resistance models accounting for the resistance components in figure 3.3 for each hull part.

	Side Hull	Keel	Torpedo
ITTC Line	ITTC 57'	ITTC 57'	ITTC 57'
Increase in frictional resistance due to hull curvature & Viscous pressure resistance	MARINTEK	MARINTEK	Hoerner 1965
Wave pattern resistance	Michell 1898 & Newman 2017	Michell 1898 & Newman 2017	Regression formula (present study)

3.3 Viscous resistance

The viscous resistance of a vessel is made dimensionless by equation (3.4).

$$C_F = \frac{R_F}{\frac{1}{2}\rho V^2 S(1+k)C_F} \tag{3.4}$$

The viscous resistance arises due to the shear force acting between the fluid and the hull. The bulk part of the viscous resistance acts tangentially to the hull surface and is called the frictional resistance. The definition of frictional resistance is presented in equation (3.5),

$$R_F = \tau S = \mu \frac{du}{dy}\bigg|_{y=0} S \tag{3.5}$$

where μ is the kinematic viscosity of water, u is the boundary layer velocity and, y is the distance from the wall in the direction normal to the wall surface, and S is the wet surface area. The velocity gradient du/dy in the boundary layer depends greatly on the flow regime, specifically whether the flow is turbulent or laminar. To identify the present flow regime, the Reynolds number is calculated by equation (3.6)

$$Re = \frac{VL}{\nu}, \tag{3.6}$$

where V is the vessel velocity, L is the vessel length, and ν is the dynamic viscosity of water. The flow around a ship model will typically be laminar for $Re < 10^5$ and turbulent for $Re > 10^7$, while a transition between the two will occur somewhere in between. A turbulent flow leads to higher shear stress at the wall and thus increased resistance than a laminar, which can be seen in figure 3.4. The laminar Blasius line is applicable for Re$< 10^6$, and the turbulent ITTC'57 line is valid for Re$> 10^7$.

in the boundary layer at the surface

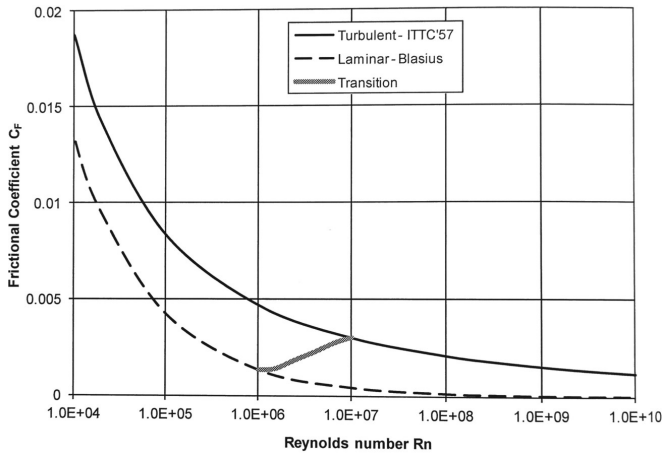

Figure 3.4: Comparison between turbulent and laminar frictional resistance models by Steen and Minsaas 2013

The vessel in the present study has Re $\approx 7 \cdot 10^6$ at 3 m/s, which is close to the intersection between the transitional regime and turbulent regime. The interval at which the flow is in the transition regime depends on the smoothness of the surface and the initial turbulence in the fluid. Since the hull material and hence the surface roughness is unknown and the initial turbulence present in the operational area is unknown, is the basis of choosing a transitional line weak. The most conservative line, i.e. the turbulent ITTC 57' correlation line is selected, and given by equation (3.7).

$$C_F = \frac{0.075}{[log_{10}(Re) - 2]^2} \tag{3.7}$$

The frictional resistance coefficient given by the ITTC 57' correlation line is only dependent on Re and does not incorporate the hull shape. As shown in equation (3.5), the frictional resistance depends on the local boundary layer velocity field, which in turn is affected by the hull shape. For instance, the velocity is increased at the shoulders of a traditional ship hull and reduced at the stagnation point at the bow. To account for the hull shape, it is common to multiply the friction resistance coefficient with the form factor (1+k). According to ITTC 2011, the ITTC 57' correlation line already accounts for a form factor based on traditional hulls. However, it is common practice to use it as a flat plate friction line and add one extra form factor.

The form factor can be determined by model trials or empirical formulas. Model tests such as Prohaska's method or low speed towing tests are time-consuming and require the construction of the ship model and testing facilities. Model tests are thus unfit for an optimisation process. The empirical formulas proposed by Holtrop 1984 and MARINTEK are based on traditional hull shapes that are different from the unconventional hull in the present paper. With the lack of other options, the two models were compared. The form

factor provided by MARINTEK is presented in equation (3.8) and can be found in Steen and Minsaas 2013.

$$\begin{aligned} k &= 0.6\phi + 145\phi^{3.5} \\ \phi &= \frac{C_B}{L_{WL}\sqrt{(T_{AP}+T_{FP})B}} \end{aligned} \tag{3.8}$$

Where C_B is the block coefficient, L_{WL} is length over the waterline, T_{AP} and T_{FP} is the draught at aft and fore perpendicular and B is the hull beam. When comparing the form factor models, it is assumed zero trim angle and thus $T_{FP} = T_{AP} = T$. MARINTEKs formula is designed to exclude the viscous pressure resistance from shedding at the aft ship. It will therefore give a lower value of k than the expected measured values from model tests. To include the viscous pressure resistance, Holtrop's formula, presented in equation (3.9) can be utilised.

$$\begin{aligned} 1 + k =& 0.93 + 0.487118 \cdot C_{14}(\frac{B}{L})^{1.06806} \cdot (\frac{T}{L})^{0.46106} \cdot (\frac{L}{L_R})^{0.121563} \\ & \cdot (\frac{L^3}{\nabla})^{0.36486} \cdot (1 - C_P)^{-0.604247} \end{aligned} \tag{3.9}$$

Where

$$L_R = L \cdot \left(1 - C_P + 0.06 \cdot C_P \cdot \frac{L_{CB}}{4C_P - 1}\right),$$

and C_{14} is a factor dependent on the hull shape and set to unity in this project. In Faltinsen 2005, typical k for high-speed monohulls is between 0.22 and 0.45 and is mainly due to the flow separation at the transom stern. The hull shape in this project does not have the sharp edge at the stern producing the flow separation. Hence k is expected to be slightly lower than what Faltinsen suggest.

To compare the form factors, an optimisation of 200 geometries was carried out, and the form factor for the 116 feasible configurations was calculated with both MARINTEK and Holtrop. A scatter plot of the comparison is presented in figure 3.5. The bulk of data points is located at 10%-20% of the expected values in Faltinsen 2005. From the figure, it is more spread in the form factors obtained from Holtrop than MARINTEK. According to Steen and Minsaas 2013 do Holtrop include viscous pressure resistance and is therefore expected to result in a higher form factor. This trend is observable for the majority of configurations, but there are several exceptions. There are even some configurations where Holtrop's form factor ended up negative, which implies reduced resistance which is unlikely. Since equation (3.9) is based on empirical values and its simplicity, it is doubtful that the spread can be justified by an accurate capture of the viscous pressure resistance. Thus, it is decided to use MARINTEK because of its consistency.

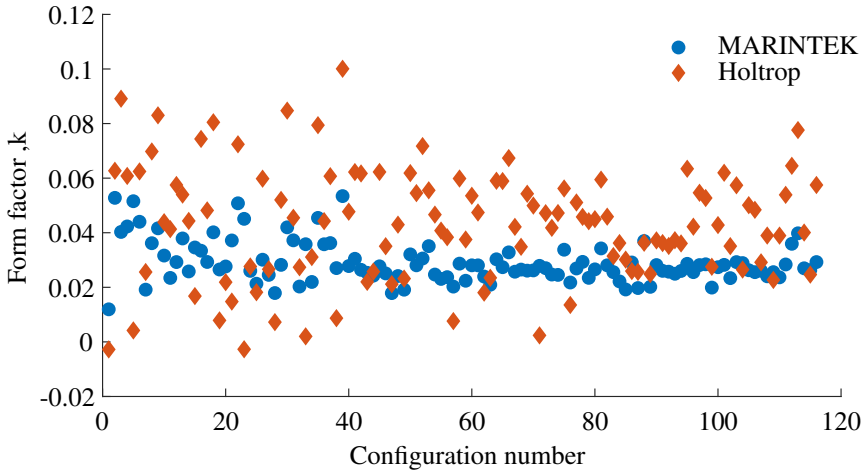

Figure 3.5: Form factor calulated with MARINTEK and Holtrop for 116 different geometries.

Hoerner 1965 introduced equation (3.10) to estimate the form factor for streamlined bodies of revolution similar to fuselages, airship bodies, nacelles etc. The generality of the formula introduces significant uncertainty to the results, as it does not account for the shape but solely the D/L ratio. However, it is assumed to give somewhat relevant results.

$$1 + k = 1 + 1.5(\frac{D}{L})^{1.5} + 7(\frac{D}{L})^{3} \tag{3.10}$$

Here, D is the diameter of the body, and L is the length of the body.

In addition to the frictional resistance mentioned so far, the viscous resistance also contains viscous pressure resistance. This resistance component arises because viscous effects lead to flow separation and generation of vortices which both inflict changes to the pressure field surrounding the hull. Concerning the geometry in the present study, it is assumed that the streamlined stern will not introduce any flow separation when the vessel has a zero yaw angle. Bow and stern vortices are likely to be present because of the infinitely sharp bilge radius. A horseshoe vortex may also arise from the intersection between the keel and the torpedo, and separation can occur at the stern of the torpedo. Because these viscous effects are highly dependent on the body shape, it is challenging to develop empirical formulas to estimate the resistance they induce. Although some form factors, such as Holtrop, contain the viscous pressure resistance, discrepancies may be introduced due to the individual geometry.

3.4 Wave resistance

Side hulls and keel

Michell (1898) developed the famous thin ship theory, a method that has been widely used to predict the wave resistance of ships since. The method is based on potential theory with source and sinks distributed along the longitudinal centre plane of the ship. The ship is assumed to be sufficiently thin thus the velocity potential from the sinks, and sources are small enough so the squared velocities can be neglected, and thus the dynamic boundary condition at the free surface can be simplified.

Tuck and Lazauskas 1998 proposed a linear superposition of the wavefield from each hull to find the combined resistance of a multihull vessel. It is considered that the energy of the waves in the wake is equal to the energy used to produce thrust, and the resistance of the vessel can thus be described by equation (3.11).

$$R_W = \frac{1}{2}\pi\rho V^2 \int_{-\pi/2}^{\pi/2} |A(\theta)|^2 cos^3\theta d\theta. \tag{3.11}$$

Here, V is the ship velocity, A(θ) is the amplitude function, and θ is the direction of propagation of the surface waves. The amplitude function can be obtained by Michell's thin ship theory, and for a single hull j, that yields equation (3.12).

$$A_j(\theta) = \frac{2}{\pi}(\frac{g}{V^2})sec^3\theta \int\int \frac{d\zeta}{dx} e^{(g/V^2)sec^2\theta(z-ixcos\theta)} dxdz. \tag{3.12}$$

Where the half beam of the ship at position (x,z) is given by $\zeta = \zeta(x,z)$, the x- and z-coordinate in equation (3.12) is the local coordinate system at the longitudinal centre plane of hull j. The amplitude function for each hull is then superposed by equation (3.13) to get the combined amplitude function.

$$A(\theta) = \sum_{j=1}^{N} A_j(\theta) e^{-i\frac{g}{V^2 cos^2\theta}(x_{j0}cos\theta + y_{j0}sin\theta)} \tag{3.13}$$

Combining equation (3.11), equation (3.12), and equation (3.13) yields the formulation of Michells thin ship theory utilised in this thesis.

Torpedo

A modification of the Michell integral was carried out by Havelock 1931 to examine a submerged ellipsoid instead of a ship hull. The resulting expression for wave resistance is given by equation (3.14).

$$
\begin{aligned}
R_W = & \frac{32\pi^2 g\rho a^2 b^2 c^2}{(2-\alpha_0)^2(a^2-b^2)^{3/2}e^{2\kappa_0}}\Bigg[\\
& \int_0^{1/\alpha} \frac{\left[\mathbf{J}_{3/2}\{\kappa_0^2(a^2-b^2)(1+t^2)(1-\alpha^2t^2)\}^{1/2}\right]^2}{(1-\beta^2t^2)^{3/2}} e^{-2\kappa_0 f t^2} dt \\
& + \int_{1/\alpha}^{\infty} \frac{\left[\mathbf{I}_{3/2}\{\kappa_0^2(a^2-b^2)(1+t^2)(\alpha^2t^2-1)\}^{1/2}\right]}{(\alpha^2t^2-1)^{3/2}} e^{-2\kappa_0 f t^2} dt\Bigg]
\end{aligned}
\tag{3.14}
$$

Where a, b and c are the three radii of an ellipsoid. κ_0 is g/V^2, β is b/a, t is $tan(\theta)$, θ is the wave propagation direction and f is the distance from the surface to the centre of the ellipsoid. $\mathbf{J}_{3/2}$ is the Bessel function of the first kind, and $\mathbf{I}_{3/2}$ is the modified Bessel function of the first kind. The constants α_0 and α are given in equation (3.15).

$$
\begin{aligned}
\alpha_0 &= abc \int_0^{\infty} \frac{dV}{(a^2+V)^{3/2}(b^2+V)^{1/2}(c^2+V)^{1/2}} \\
\alpha &= \sqrt{(b^2-c^2)/(a^2-b^2)}
\end{aligned}
\tag{3.15}
$$

Early in the design stage, equation (3.14) was used to estimate the wave resistance of the torpedo but the error introduced by approximating the torpedo as an ellipsoid motivated the pursuit of a new approach. Papers on the wave resistance of torpedo shapes exist in the literature, but the data basis usually lack a sufficient number of submergence ratios, or the geometry is slightly different. One of the examples can be found in Hoerner 1965, who used the experimental results from Weinblum, Amtsberg, and Bock 1936 and plotted the wave resistance coefficient against the submergence ratio h/L, shown in figure 3.6. The data points marked "*" refer to the torpedo shape in the same figure, and is interpolated to find the wave resistance coefficient of the present torpedo. However, the torpedo shape in figure 3.6 is more streamlined than the present torpedo, and the data points are only given for length Froude number 0.4. It is therefore decided to establish a regression model based on CFD simulations, to get a more confident estimate of the wave resistance.

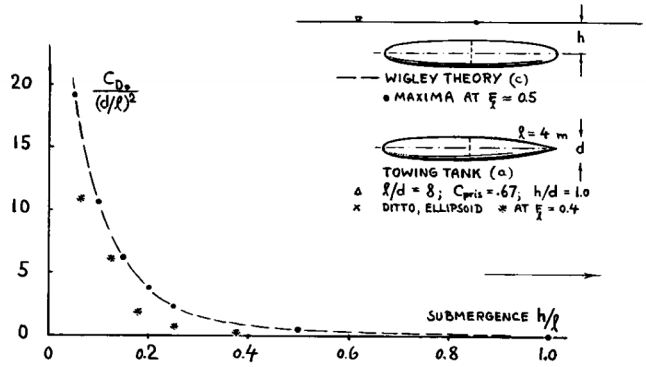

Figure 3.6: Drag coefficient for submerged bodies of revolution, taken from Hoerner 1965.

It was decided to keep the length-to-diameter ratio L/D constant to limit the parameters in the regression formula. The decision on L/D ratio is based on the work by Moonesun et al. 2016, who carried out CFD-simulations for 11 submarine shaped bodies with different L/D ratio. As expected, high L/D resulted in severe friction resistance, while low L/D resulted in severe pressure resistance. For cylindrical middle body submarines, Moonesun et al. suggested the optimum range of L/D to be between 7 and 10. It was also observed that the total resistance increased remarkably faster when L/D was reduced below 7 compared to when it exceeded 10. It was therefore decided to use L/D=10 in this project, and the length of the cone is set to 1.5D.

A set of simulations of the torpedo with varying size and submergence ratio h/D were carried out and presented in table 3.2, with the geometry of the torpedo shown in figure 3.7. The pressure resistance from the CFD simulations are also given in the table in addition to the wave resistance of an ellipsoid from Havelock 1931 and torpedo from Hoerner 1965. The maximum free surface displacement in all three simulations with h/D=5.5 was below $5 \cdot 10^{-3}$m hence the wave resistance is close to zero. The pressure resistance in these three simulations is, therefore, essentially the viscous pressure resistance that arises due to separation at the stern. The separation is visible in where the velocity is plotted for the largest torpedo at h/D=5.5.

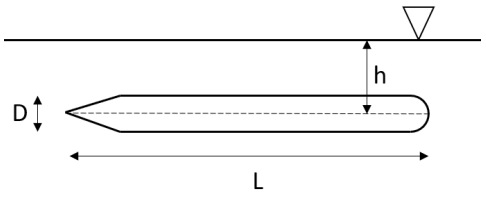

Figure 3.7: Parameters describing the torpedo geometry.

Table 3.2: CFD simulations of torpedo at various size and depth-to-diameter ratio with corresponding pressure resistance from CFD simulations, wave resistance with equation (3.14) from Havelock 1931 and wave resistance from figure 3.6 obtained from Hoerner 1965. All the simulations are carried out at 3m/s.

L [m]	D [m]	h/D [-]	Pressure CFD [N]	Havelock 1931 [N]	Hoerner 1965 [N]
2	0.2	0.5	32	22	43
2	0.2	1.0	21	13	22
2	0.2	1.5	16	8	8
2	0.2	2.0	14	5	4
2	0.2	5.5	10	1	1
3	0.3	0.5	88	113	94
3	0.3	1.0	64	60	48
3	0.3	1.5	43	34	18
3	0.3	2.0	30	20	9
3	0.3	5.5	22	1	2
4	0.4	0.5	163	225	164
4	0.4	1	104	117	84
4	0.4	1.5	67	63	31
4	0.4	2.0	51	36	15
4	0.4	5.5	30	1	3

As expected, particularly because of the different geometry, there is varying resistance between the three methods. The results are compared by plotting the residual resistance coefficient against the depth-Froude number in figure 3.8. The plots show similar behaviour for all methods, and the coefficients obtained are in the same bulk part. Except for the cases with h/D=5.5, Havelock 1931 overestimates C_R by 56.7% at most and Hoerner 1965 overestimate by 34.3% at most compared to CFD.

It is therefore decided to use the results from CFD to establish a regression formula that will be utilised in the optimisation of the torpedo. Since free water waves decrease exponentially with depth, the terms related to the draught is chosen as an exponential function. The terms related to the diameter are also related to the length since the aspect ratio is kept constant. The wave resistance is dependent on the Froude number, and the Froude number is dependent on $L^{-1/2}$. The diameter is therefore expressed by a quadratic function in the regression formula. The combined regression formula for the residual resistance is given by equation (3.16) and its coefficients in table 3.3.

$$R_R = c_1 + c_2 D + c_3 D^2 + c_4 D e^{C_5 T/D} + c_6 D e^{C_5 T/D} \tag{3.16}$$

c_1	c_2	c_3	c_4	c_5	c_6
-60.77	156.9	18.10	559.6	-1.205	-93.27

Table 3.3: Constants used in the curve fitting equation (3.16)

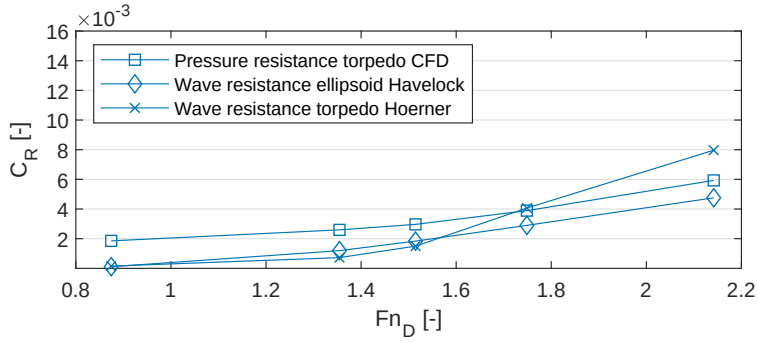

(a) L=2m

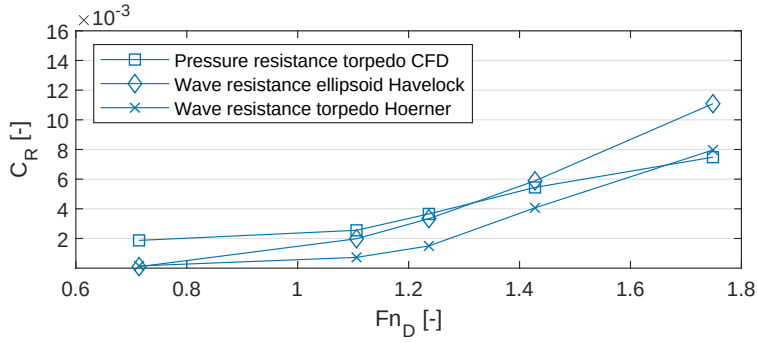

(b) L=3m

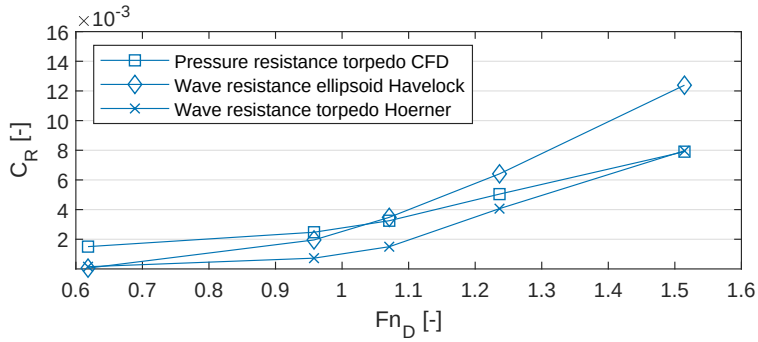

(c) L=4m

Figure 3.8: Comparison between residual resistance coefficient obtained from three different methods. The comparison is carried out for three different torpedo sizes, L=2m(a), L=3m(b) and L=4m(c) and all have L/D=10. Fn_D is the depth Froude number.

The regression fits the data points from CFD well, with R-square value 0.9966 and root mean square error of 3.033. The data points from the CFD simulations and Havelock is plotted with the surface given by equation (3.16) in figure 3.9.

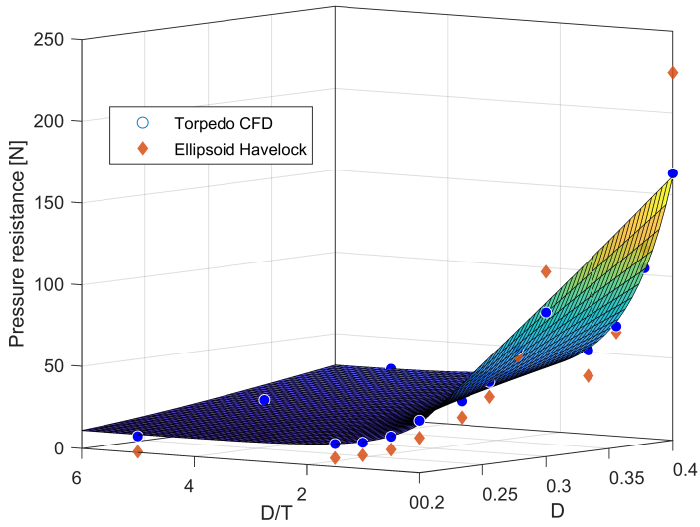

Figure 3.9: Pressure resistance for torpedoes at 3 m/s with L/D=10 close to the free surface. Blue circles are from CFD simulations, red diamonds are ellipsoids from Havelock 1931 and the surface is given by equation (3.16).

Transom stern

It is investigated the possibility of constructing the side hulls with a transom stern. The submerged volume that initially was in the pointy stern is compensated for by widening the hull or increasing the draught slightly, and both will result in smaller wet surface than the pointy stern. Hence, the advantage of a transom stern is a reduction in frictional resistance due to the reduced wet surface. However, the transom stern will introduce a base drag that may exceed the saves in frictional resistance.

The magnitude of the base drag can be challenging to establish and is normally accounted for by either the form factor or a base drag coefficient, the latter can be determined by equation (3.17) according to Steen 2014.

$$C_{BD} = \frac{D_B}{\frac{1}{2}\rho V^2 S} = 0.029\sqrt{\frac{(\frac{S_B}{S})^3}{C_F}} \tag{3.17}$$

In equation (3.17) is S_B the area of the transom stern below the waterline and S is the remaining wet hull area. However, when the velocity becomes sufficiently large, the back-flow in the wake is not keeping up with the vessel, and the transom stern becomes dry. Sufficiently large velocity is an ambiguous term and according to Steen and Minsaas 2013 have typical displacement ships a wet transom for F$_n$¡0.20.$Sincethevesselinthisthesisisisnotatypicaldispl$

$$R_{transom} = \rho g \int_0^H zB(z)dz \tag{3.18}$$

Where H is the maximum draught of the transom and B(z) the width of the transom at different draughts.

A new and more sophisticated approach is introduced by Doctors and Day 2001, who managed to develop a computer program that iterates the hollow behind a high-speed vessel until the atmospheric pressure condition is satisfied at the surface of the hollow. However, the method requires the computation of the near-field solution that introduced far more complexity to the problem. To reduce the complexity of the problem, it was decided to install streamlined rudders instead of transom sterns. This decision were made after the validation cases were constructed, hence some of the validations are carried out for transom sterns and some are not.

3.5 Hull optimisation

With the resistance models aforementioned, the total resistance of the vessel can be estimated fast enough to carry out an optimisation. The seven parameters that are optimised are listed in table 3.4 and visualised in figure 3.2. Initially, the constraints were only a displacement of 200kg and a maximum length of 3m. However, the problem is ill-posed since the lowest resistance is obtained when the side hulls have close to no submergence, i.e. less than 1 cm. The reason is the diminishing wave resistance from the side hulls when the draught is so small. This is in itself unproblematic. However, the troubles arise due to the limited righting moment.

In the project thesis preceding this master thesis, a simplified investigation of the transverse stability is carried out. For a pure roll motion, the righting arm, GZ, will increase substantially when the roll angle increases while both side hulls are partly submerged. This is illustrated by condition A in figure 3.10. The reason is an increase in roll angle transfer some of the submerged volume in one of the side hulls to the other and thus shifting the centre of buoyancy horizontally to the most submerged side hull. In condition B, When one of the side hulls are out of the water, increasing the roll angle will not have any significant effect on the centre of buoyancy and GZ will actually decrease gently. When the torpedo exits the water in condition C it leads to an increase in GZ, as the submerged volume is transferred from the torpedo to the side hull. Finally, in condition D is the side hull the only submerged part and GZ reduces as the roll angle increase.

The pure roll motion described above is highly unlikely to happen in a real scenario as the sail and hydrodynamic forces will usually be in equilibrium at a non zero trim and yaw angle as well. It is only mentioned to grasp the straight forward effects on transverse stability. There are observed two significant influences on the righting moment. The first is; the greater the submerged volume in the side hulls the greater initial stability. The second is rather a criterion; the total volume of one side hull needs to be greater than the total displacement of the vessel, to get the increase in GZ in the condition D. A safety factor was added so the volume of each side hull is 1.5 times the total displacement of the vessel, this is done by determining the height of each side hull.

If the righting moment is limited, the vessel will obtain a roll angle when the external forces act on the vessel. The roll angle will subsequently increase the draught of one of the side hulls leading to a significant increase in wave resistance.

It is chosen to establish a highly simplified stability condition, with the only intention of excluding the designs with extremely small submergence from the optimisation. The proposed solution is to require the righting moment between condition A and B in figure 3.10 to withstand the roll moment from the sail at a specified wind velocity.

In an attempt to quantify the external force that the vessel will experience, data from Harstveit 2005 was used. Harstveit provided a graph showing the percentiles of wind speed each year from 1955 to 1997 at three different locations; The North Sea, The Norwegian Sea and the Barents Ocean. The trend of the 0.99 percentile is slightly above 20 m/s, and the 0.95 percentile is about 17-18 m/s. Hence, if the boat is designed to withstand wind of 20 m/s, it should be able to operate in the majority of the time.

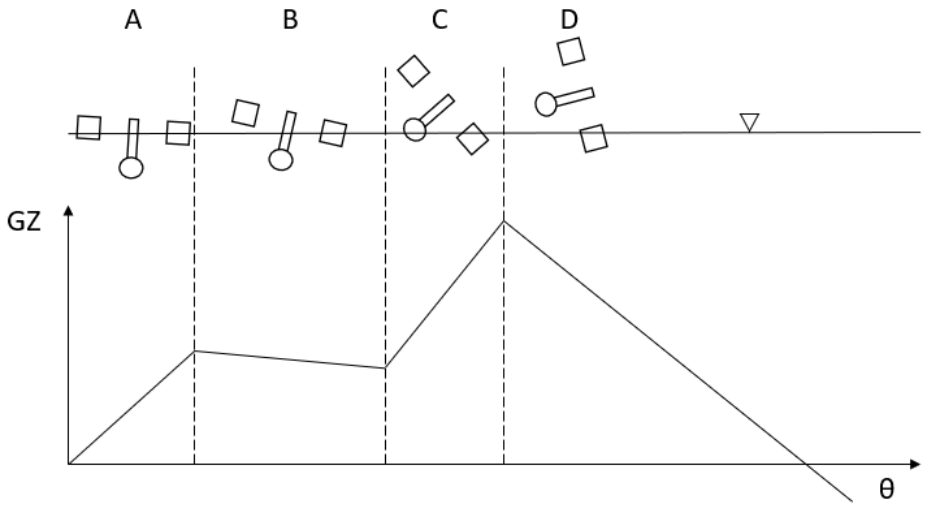

Figure 3.10: Generic GZ-curve for the present hull.

Table 3.4: Optimisation parameters, constraints and goal

		min	max
Optimisation parameters	L Side hull	2.0 m	3.0 m
	B Vessel	1.5 m	2.5 m
	B Side hull	0.05 m	0.6 m
	L Keel	0.2 m	2.0 m
	B Keel	0.05	0.3 m
	H Keel	0.0 m	1.0 m
	D Torpedo	0.1 m	0.3 m
Constraints	Displacement	200 kg	
	Velocity	3 m/s	
	Displacement side hull	Equation (3.22)	
Goal	Resistance	Minimize	

The roll moment from the sail is roughly approximated by multiplying the lift force with the sail moment arm. The lift force is estimated by equation (3.19) and the moment arm is the vertical distance from the centre of gravity of the vessel to the centre of pressure(COP) of the sail. Since the sail design is investigated by one of the other master's thesis in the current project, the sail parameters in table 3.5 will be used without justifications. This procedure introduces several simplifications, firstly that the lift force is acting in the exact transverse direction and the drag force is neglected. Secondly, that the wind is uniformly distributed along the sail span. Finally, the roll and trim angle inflicted by the sail force is neglected and thus over predicting the lift force.

$$L = 0.5\rho_{air}V_{wind}^2 SC_L \tag{3.19}$$

The correct righting moment at a given wind speed and direction can be found by integrating the submerged volume to determine the centre of buoyancy. Then multiplying the buoyancy force with GZ will give the righting moment. The integration, however, is not straight-forward since iteration of roll, trim and yaw angles are needed to balance the sail moment and the righting moment. A reasonably simple model is utilised instead.

Assuming small roll angles, increasing the roll angle slightly will reduce the submerged volume of one side hull by the same amount as the other will increase. The centre of gravity remains unchanged while the centre of buoyancy is shifted horizontally in the direction of the submerging side hull. Let the fraction of displacement of one side hull to the displacement of the entire vessel be denoted $\frac{\nabla_{SH}}{\nabla_{tot}}$ at zero roll angle. Then, the centre of buoyancy (COB) has approximately a lateral position according to equation (3.20) when the side hull exits the water.

$$COB \approx \frac{\nabla_{SH}}{\nabla_{tot}} B_{vessel} \tag{3.20}$$

Let COG be in origo so COB≈GZ, then the corresponding righting moment is given by equation (3.21).

$$M = L \cdot COP \approx \nabla \cdot COB \approx \rho g \nabla_{SH} B_{vessel} \tag{3.21}$$

Hence the displacement of one side hull needs to fulfil equation (3.22).

$$\nabla_{SH} \geq \frac{M}{\rho g B_{vessel}} \tag{3.22}$$

For example, if the wind speed is 20 m/s and the vessel is 2m wide, the sail moment becomes 1910Nm, and the displacement of the side hull needs to be $0.95m^3$. In other words, both side hulls will account for 97% of the vessel displacement, which implies that the torpedo and keel will have to be extremely small. As a result, the boat have to be wider, the moment arm of the sail decreased, or the wind speed decreased in order to avoid large roll angles.

It is concluded that the wind velocity of 20m/s is greater than what can be expected as an operating condition; hence the wind velocity is reduced to 15 m/s. The roll moment is then approximately 1kNm, and the needed side hull displacement is reduced to approximately 50% of the total displacement. That is more feasible than for 20 m/s and still covers somewhere between 75% and 95% of the expected wind according to Harstveit 2005.

PSO

To optimise the vessel in regard to resistance, it is chosen to use Particle Swarm Optimisation due to its applicability to multidimensional and non-differential problems. There are numerous variants of the PSO algorithm, and it is decided to use the standard version developed by Kennedy' and Eberhart 1995 accompanied by a penalty function.

A vector containing 40 applicable values is created for each optimisation parameter. The values are evenly spaced within the limits presented in table 3.4. The number of possible combinations is, therefore, $40^7 \approx 1.6 \cdot 10^{11}$. The swarm size, i.e. number of particles, is set to 200 and the number of generations is set to 10.

First, a set of initial particles is created with random combinations of the optimisation parameters. The objective function f(X), i.e. the resistance of the vessel, is then computed for every particle. To account for the constraint in table 3.4, a penalty function P(X) is introduced similar to the penalty function in Homaifar, Qi, and Lai 1994. The constraint function g(X) given in equation (3.23) is a rephrasing of the equation (3.22), such that g(X) takes a value between 0 and 1 if the constraint is violated. Particularly, if the side hull is not submerged at all g(X)=1 while the closer equation (3.22) is to be fulfilled the closer g(X) will be zero.

$$g(X) = 1 - \frac{\rho g B_{vessel} \nabla_{SH}}{M} \tag{3.23}$$

Additionally, if g(x)>0 the particle will be removed as a candidate for $gbest$ which is the best-known position so far, and a penalty function P(X) is introduced to the objective function f(X). The penalised objective function F(X) is then expressed in equation (3.24).

$$F(X) = f(X) + P(X) \tag{3.24}$$

$$\begin{cases} P(X) = 0 & g(X) < 0 \\ P(X) = g(X)R & g(X) > 0 \end{cases} \tag{3.25}$$

The R in equation (3.25) is a penalty factor that scales the penalty function. The most fitting value of R varies from problem to problem and is difficult to determine. If it is too low, a particle will have difficulties to leave a local minimum that violates the constraint. Contrarily, if it is too high, there is a greater chance that the global minimum will be undiscovered if its position is close to the constraint. With the penalised objective function obtained the velocity is then calculated for every particle in each dimension by equation (3.26).

$$U_{ij}^{t+1} = wU_{ij}^{t} + c_1 r_1^t (pbest_{ij} - X_{ij}^t) + c_2 r_2 (gbest_j - X_{ij}^t) \tag{3.26}$$

Where the subscript i refer to particle number, j refer to the dimension. The t represents the iteration number, the inertia w is set to 1.4 and the initial velocity $V_{i,j}^1 = 0$. The constants $c1$ and $c2$ are both set to 2, which Kennedy' and Eberhart 1995 found to be the most favoured choice. The factors r_1^t and r_2^t are random numbers between 0 and 1. The best position a single particle has detected so far is denoted $pbest_i$, and the current position in dimension j is denoted X_{ij}^t. The new position of each particle is subsequently calculated by

$$X_{ij}^{t+1} = X_{ij}^t + V_{ij}^{t+1} \tag{3.27}$$

There is no guarantee that the outcome of the optimisation is the best possible combination of optimisation parameters, even though the objective value has converged. The reason is that local minimums can attract the particles and prevent the global minimum from being discovered.

3.6 CFD

To construct the VPP, several hydrodynamic coefficients are needed. These coefficients were obtained by running CFD simulations with varying roll, pitch and yaw angles using STAR CCM+. A list of the simulations conducted can be found in table 5.2.

Geometry

The computational domain consists of six outer boundaries; one inlet, one outlet and four sides parallel to the flow. The boundary condition for the outlet is pressure outlet while the inlet, top and bottom have velocity inlet as the boundary condition. The boundary condition at the sides is symmetry walls. The domain is 96m x 64m x 12m and visualised in figure 3.11. In the resistance predictions, the mesh convergence, and the trim conditions are the domain halved in the longitudinal direction to reduce the computational cost. However, when roll and yaw angles are introduced, the geometry becomes asymmetrical with respect to the x-z plane. Thus, the entire domain in figure 3.11 have to be utilised.

Physics

The viscous effects of the flow around the vessel are of great interest. First of all, the friction that the vessel experience is essential for the resistance prediction. Secondly, what is more difficult to predict with empirical formulas is the flow separation and vortex production around the sharp corners. To capture these effects, a turbulence solver has to be included.

Direct Numerical Simulation was out of the question since it demands too much computational power. Large Eddy Simulation and Detached Eddy Simulation resolve the large scale eddies but models the smaller eddies in the near-wall region and are therefore computational costly without improving the near-wall turbulence that is of interest in this project.

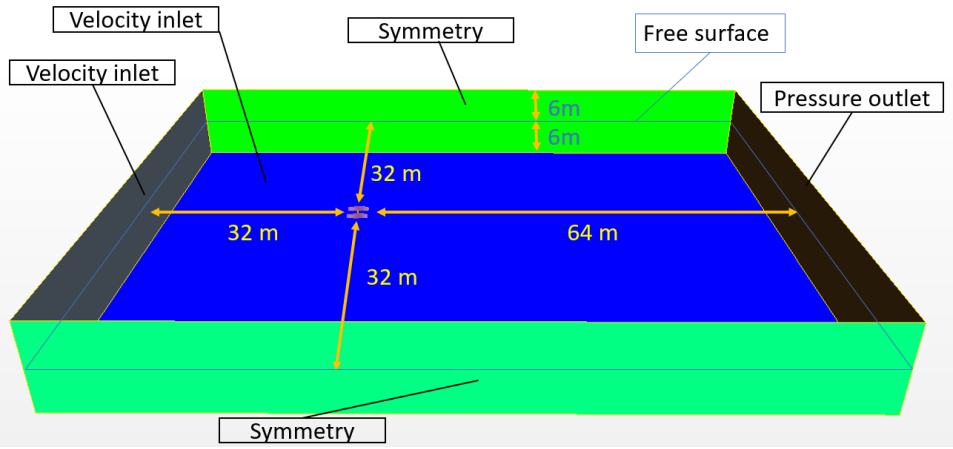

Figure 3.11: Computational domain for yaw and roll simulations, presented with boundary conditions and dimensions.

Spalart-Allmaras is robust but has limitations to shear flows and separated flows. The preferred models that balance computational cost and accuracy are the two-equation RANS models. The SST Menter turbulence model was selected, which is a combination of the k-ϵ and k-ω. The model use k-ω near the wall to get an adequate representation of boundary layer close to the wall, and k-ϵ in the free stream flow to avoid the free stream sensitivity of the k-ω model. The free surface was modelled with the Volume of Fluid (VOF) solver. The buoyancy was corrected for by using the Dynamic Fluid Body Interaction (DFBI) model with free motion in the z-direction. The motion was frozen for the first ten time steps for stability reasons. The vessel is observed oscillating in heave, hence he Baumgarte constraints α was adjusted from 5 to 15 and β kept at 20 to damp the movement.

Mesh

The mesh was constructed using hexahedral cells. A volumetric control was added at the free surface to make sure the undisturbed free surface lays on the face between two cells, to avoid the interface to be smeared. A two-step refinement was added in a trapezoidal area around the vessel to resolve the divergent and transverse waves properly. The first and finest is two times Lpp long, and the second and coarser one is six times Lpp long.

A mesh convergence study is carried out for eight different cell refinements. The increase in mesh size is done by changing the base size of the mesh, hence scaling all cells equally. The only exception is the prism layers close to the wall, which is kept constant for all refinements and its properties are specified later in this section. Additionally, is the dimension of the vessel region adjusted to fit around the vessel without an excessive amount of cells between the vessel and the overset boundary.

The results of the convergence study are plotted in figure 3.12, where the resistance drops rapidly until approximately 1M cells. Above 1M cells, the change in resistance is less;

however, a smooth convergence is not observed. It is decided to continue with the $\approx$ 2.6M refinement since the 5.3M refinement is too computational costly for the hardware available and to stay clear of the rapidly changing region below 1M.

To manage the DFBI motion, an overset mesh was used to account for the moving mesh. The domain was divided into a background region and a vessel region. The background region was stationary and consisted of the box in figure 3.11. The vessel region consisted of the vessel hull itself and an enclosing box just outside of the hull. The overset mesh was then interpolating data between the boundary of the background region and the vessel region. To ensure a good interpolation between the region, the mesh size at the outer boundaries of the vessel region is uniform. A mesh refinement in the background mesh was done with the same cell size as the outer boundary of the vessel region. This mesh refinement span a minimum of four cells outside of the vessel region in all directions. Additionally, it was made sure to follow CD-adapco's best practice of using a minimum of four cell layers between the body in the vessel region and the overset boundary.

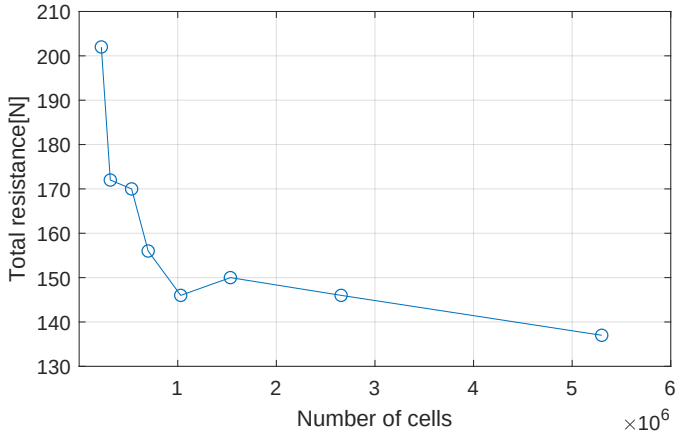

Figure 3.12: Mesh convergence

In the near-wall region, the solution gradients are very high and need special treatment to be correctly modelled. The two prominent solutions are wall functions and near-wall modelling. Wall functions use the predicted dimensionless boundary layer profile to estimate the velocities in the viscous sub-layer and the buffer-layer. While the near-wall modelling involves a mesh refinement in the viscous sub-layer and buffer-layer and subsequently resolve it.

The benefit of wall functions is the reduced amount of cells and computational time. However, since the drag is essential in this study, the more accurate near-wall modelling is chosen. A prism layer is therefore included in the mesh adjacent to the hull surface. To get a proper solution, the first cell needs to be in the viscous-sublayer, which is the part of the boundary layer that is closest to the wall. The viscous forces are so dominant in this region that the flow that the Reynolds shear stress is negligible. Outside of the vis-

cous sub-layer is the buffer layer, where the transition from the viscous dominated flow to the turbulence dominated flow occur. Neither of the viscous shear stress or turbulent shear stress can be ignored, and there exists no universal law for the composition of the two, it is, therefore, essential to place the first layer outside this region. To determine what distance corresponds to the laminar sub-layer, the y+ value need to be determined by equation (3.28).

$$y^+ = \frac{yu_\tau}{\nu} \tag{3.28}$$

Where y is the distance from the wall, u_τ is the friction velocity and ν is the kinematic viscosity. The friction velocity is given by equation (3.29)

$$u_\tau = \sqrt{\frac{\tau_w}{\rho}} \tag{3.29}$$

with τ_w being the wall shear stress given by equation (3.30), where U_∞ is the free stream velocity.

$$\tau_w = 0.5\rho C_F U_\infty^2 \tag{3.30}$$

The skin friction coefficient is determined by equation (3.7). The non-dimensional distance y^+ is then used to reveal in which of the sublayers the individual cell is positioned. It is known that the range of the laminar sub-layer is $0 < y^+ < 5$, buffer-layer is $5 < y^+ < 30$ and the log-law region is $30 < y^+$. That implies accordingly that the thickness of the first cell needs to be less than y^+=5, and good practice is y^+=1 and thus aimed for in the present study. Inserting L=3m, V=3m/s and ν=1$\cdot 10^{-6} m^2/s$ in equation (3.6) result in Reynolds number 9$\cdot 10^6$, and subsequently $C_F = 3.1 \cdot 10^{-3}$ from equation (3.7). Solving equation (3.28) for $y^+ = 1$ result in the prism layer being closest to the wall will have a thickness of $y = 8.5 \cdot 10^{-6} m$.

It is recommended to have at least ten prism layers in the buffer-region and preferably more. Due to the limited computational power and shortness of time, the number of prism layers is kept at 10 for all simulations. The prism layers follow a growth rate of 1.4 resulting in the outermost layer having y+$\approx$70 and the total accumulated thickness of the prism layers becomes $5.9 \cdot 10^{-4}$.

The mesh with $\approx 2.6M$ cells is visualised in figure 3.13.

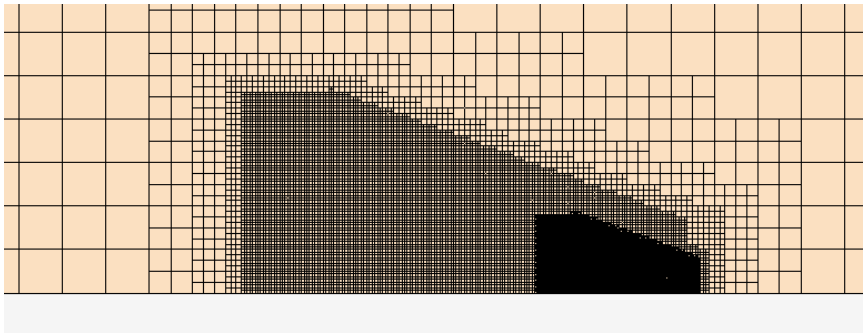

(a) View from above with the coarse and fine refinement zones of the wake

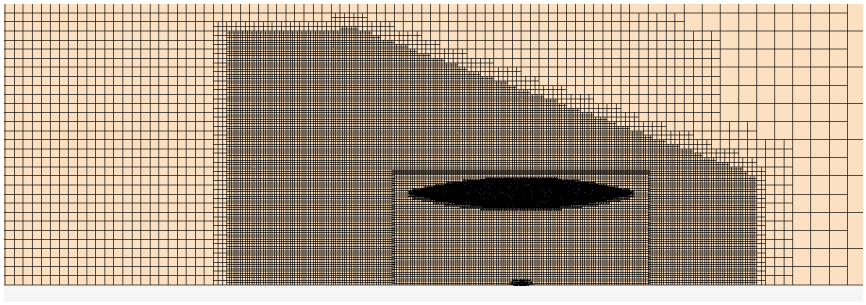

(b) The fine refinement zone viewed from above

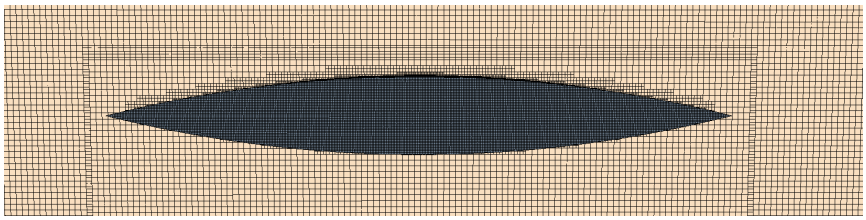

(c) The side hull seen from above with the overset mesh boundary just outside of the hull

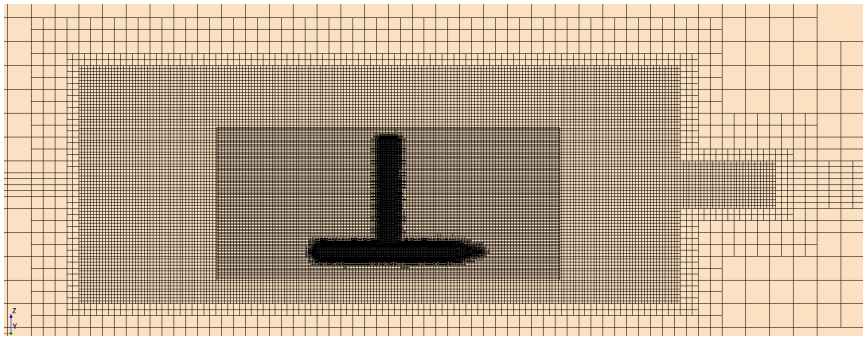

(d) Side view of the centre plane. The box surrounding the keel and torpedo is the vessel region and its edge is the overset mesh boundary. At the far left and right is the free surface refinement visible.

Figure 3.13: Visualisation of the mesh with ≈2.6M cells

3.7 VPP

General definitions

A basic Velocity Prediction Program (VPP) is written in MATLAB to estimate the performance of the vessel for the input variables; wind speed and wind direction. Briefly, the program calculates the forces and moments induced by the wind and balance them against hydrodynamic forces and moments generated by the hull until equilibrium is achieved. The velocity and orientation of the vessel are finally given as the output.

Since the sea keeping abilities are not considered in the present study is the heave motion absent, i.e. $V_z = 0$. A constant sway motion is equivalent to a constant yaw-angle; hence only one of them is necessary, and the latter is chosen. The velocity of the vessel can, therefore, be decomposed to $V_x = -Vcos\psi$ and $V_y = Vsin\psi$. The force balancing is then carried out for five unknowns; Velocity (V), roll (ϕ), trim (θ), yaw (ψ), and rudder angle β. The rotations are visualised in figure 3.14 and the velocity is visualised in figure 3.15.

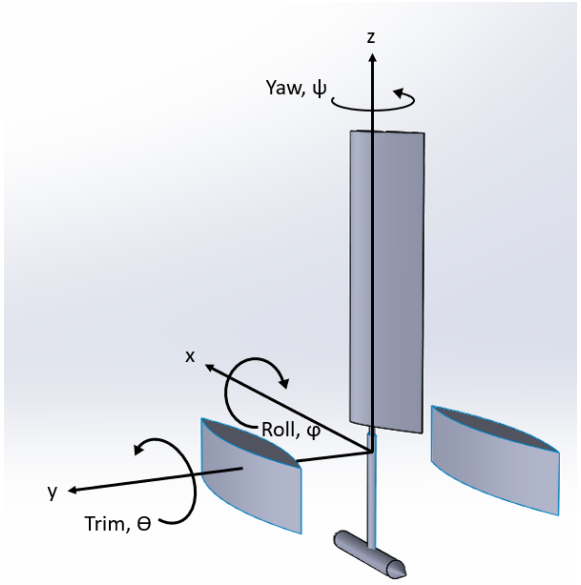

Figure 3.14: Axis system and roll, trim and yaw definitions.

The sail arrangement is considered in another master thesis; hence the design parameters will be used here without justification. Unlike traditional sails, it is a solid body with a constant cross-section and properties presented in table 3.5. The sail can rotate 360 degrees around the z-axis to obtain the angle of attack which produce maximum thrust during transit or minimum force during a storm.

Table 3.5: Sail properties

Parameter	Value	Unit
Profile	NACA 0018	
Span	2.4	m
Chord length	1.2	m
Projected area	2.88	m^2
Weight	4.5	kg

Forces

The lift (L) and drag (D) acting on the sail are determined by equation (3.31).

$$\begin{aligned} L &= 0.5\rho_{air}AC_L V_{wind}^2 \\ D &= 0.5\rho_{air}AC_D V_{wind}^2 \end{aligned} \tag{3.31}$$

Where ρ_{air} is the air density, A is the foil surface area and V_{wind} is the wind velocity. The lift and drag coefficients C_L and C_D are provided by the master thesis focused on the sail in the range of $-20 \geq \alpha \leq 20$. The lift and drag force are thus calculated for each of the 41 degrees and transformed into x'- and y directions. Since maximum thrust is desired is the angle with the largest corresponding force in x-direction chosen to be the sail angle. M_x and M_y are then calculated by multiplying the respective sail force with the distance from the centre of gravity to the centre of pressure on the sail. It is assumed that the centre of pressure is positioned on the middle of the sail in the span direction. The effect of ϕ and θ on the effective sail area is not taken care of. The wind force on the hull is also neglected.

To reduce the complexity of the CFD simulations is the rudder omitted in all simulations and replaced with a fixed pointy stern as in figure 3.14. However, the rudder is central in balancing the moment M_z thus a simplified representation of the rudder is added to the VPP program. A symmetric foil is positioned at the stern of each side hull as in figure 3.1, with an angle β to the centre-line of the side hull. The lift and drag from the foils are calculated by equation (3.31) and decomposed to x' and y' direction. For simplicity reasons, it is assumed the force always acts 1/4 of the cord length behind the leading edge. Finding the induced moment M_z from the rudder is then straight forward multiplying the force F_y from the rudder with the longitudinal distance between the rudder force and vessel centre of gravity. The cord length of the rudders is set to 0.25m and the thickness required to get a smooth transition to the surrounding hull is 0.045m which corresponds to 18%. The closest match to this geometry is the EPPLER 473 airfoil that has a thickness ratio of 16.2%, so the C_L and C_D curve for the rudder is retrieved from this foil.

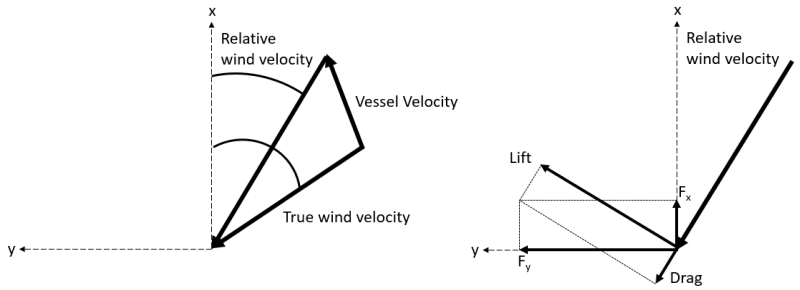

(a) True and relative velocity

(b) Sail forces

Figure 3.15: (a)Definition of wind true wind direction and relative wind direction.(b)Decomposition of sail forces

Computational structure

The loads from the sail are then balanced with the hydrodynamic loads until equilibrium is achieved. The hydrodynamic loads are determined by equation (3.32),

$$\begin{bmatrix} F_x \\ F_y \\ M_x/B \\ M_y/L \\ M_z/L \end{bmatrix} = \frac{1}{2}\rho V^2 \mathbf{C} S + \frac{1}{2}\rho \mathbf{C_0} S \tag{3.32}$$

where the vectors $\mathbf{C}$ and $\mathbf{C_0}$ is defined by equation equation (3.33). A complete list of the coefficients used in equation (3.33) can be found in section 5.2.

$$\mathbf{C} = \begin{bmatrix} C_{F_x}(\phi) + C_{F_x}(\theta) + C_{F_x}(\psi) + C_T \\ C_{F_y}(\phi) + C_{F_y}(\psi) \\ C_{M_x}(\phi) + C_{M_x}(\psi) \\ C_{M_y}(\phi) + C_{M_y}(\theta) + C_{M_y}(\psi) \\ C_{M_z}(\phi) + C_{M_z}(\psi) \end{bmatrix} \qquad \mathbf{C_0} = \begin{bmatrix} 0 \\ 0 \\ C_{M_x,0}(\phi) \\ C_{M_y,0}(\theta) \\ 0 \end{bmatrix} \tag{3.33}$$

The first step is to determin the sail forces with zero roll, trim and yaw angle. The the vessel velocity and relative wind velocity is determined. Subsequently, is the initial value of V_x is estimated by setting the sail force in x-direction equal to R_T in equation (3.2) and C_T is obtained from the CFD simulations. Then the initial values of ϕ, θ and ψ are estimated by calculating the associated coefficient that corresponds to the given sail force. That is, F_x is balanced with V, F_y is balanced with ψ, M_x is balanced with ϕ and M_y is balanced with θ. For instance, the initial trim coefficient C_{M_y} is found by equation (3.34).

$$C_{M_y} = \frac{-M_{y,wind}}{0.5\rho S V^2}. \tag{3.34}$$

After the coefficients are obtained is the corresponding angle determined by interpolation/extrapolation of the CFD data. A consequence of the motion being coupled is the non-zero net load obtained with the angles so far. Hence, the iteration of the four unknown is carried out with Newton Raphson method presented in equation (3.35).

$$x_{n+1} = x_n - \frac{f(x_n)}{f'(x_n)}. \tag{3.35}$$

Here, x is one of the degrees of freedoms, i.e. V, ϕ, θ, ψ or β and f is the net load in the respective direction. The derivative in equation (3.35) is found by equation (3.36), thus two initial values are needed for every degree of freedom.

$$f'(x_n) = \frac{f(x_n) - f(x_{n-1})}{x_n - x_{n-1}} \tag{3.36}$$

The second initial value for the velocity is obtained by equation (3.37), and similarly for the four other DOFs.

$$V_n = V_{n-1}\ sgn(F_{x,hydro} + F_{x,wind})\ \sqrt{\left|1 + \frac{F_{x,hydro} + F_{x,wind}}{F_{x,wind}}\right|} \tag{3.37}$$

At first, a loop where every degree of freedom was iterated successively were constructed. However, it is experienced that the coupling effect is severe enough to prevent the iteration from convergence by doing so. To fix this, there is only one degree of freedom that is iterated for each loop. The chosen degree of freedom is always the one with the largest difference between the hydrodynamic loads and the wind loads. The difference is calculated for each loop, and when the sum of difference for all degrees of freedom becomes less than 1 N or Nm, the solution is approved, and the wind direction is increased by one increment. The process is then repeated for the desired amount of wind directions and subsequently, the desired amount of wind velocities.

Hydrodynamic coefficients

The forces from CFD is non-dimensionalised by introducing a set of coefficients. These coefficients are in general found by equation (3.38) for forces and moments.

$$\begin{aligned} C_{F_i} &= \frac{F_i}{\frac{1}{2}\rho V^2 S} \\ C_{M_i} &= \frac{M_i}{\frac{1}{2}\rho V^2 S L} \end{aligned} \tag{3.38}$$

F_i is the load in direction i, V is the absolute velocity magnitude of the vessel, S is a reference area, and L is a reference length. As stated above, the vessel has a total of five unknowns, while the rudder angle is omitted in the CFD simulations and the velocity is accounted for by equation (3.38), it is only necessary to determine coefficients based on ϕ, θ and ψ. Thus the number of coefficients amounts seemingly to 15, yet some can be omitted, and some need further disintegration into static and dynamic contributions.

Due to symmetry is $C_{F_y}(\theta) = 0$, $C_{M_x}(\theta) = 0$ and $C_{M_z}(\theta) = 0$. It should be mentioned that this is only true when $\psi = 0$. For instance, it is obvious that θ has a great impact on M_z if $\psi \neq 0$. This introduces a large weakness to the VPP, as the coefficients are only determined for uncoupled motions in the CFD simulations.

Further, $C_{M_y}(\theta)$ is separated into a dynamic component and a stationary component. The reason being the hydrostatic moment that is independent of velocity account for the majority of the righting moment. The coefficient $C_{M_y,0}(\theta)$ are therefore introduced as the static moment coefficients with the unit $\frac{1}{s^2}$, calculated by equation (3.39). The same would be true for $C_{M_x}(\phi)$ but due to limited time, it is not simulated roll without a velocity. Since it is assumed the majority of the righting moment originate from hydrostatics, the magnitude of $C_{M_x}(\phi)$ is transferred to $C_{M_x,0}(\phi)$, and subsequently $C_{M_x}(\phi)$ is set to zero.

$$C_{M_i,0} = \frac{M_i}{\frac{1}{2}\rho S L} \tag{3.39}$$

The complete expression for M_y then becomes

$$M_y = \frac{1}{2}\rho V^2 S(C_{M_y}(\phi) + C_{M_y}(\theta) + C_{M_y}(\psi)) + \frac{1}{2}\rho S C_{M_y,0}(\theta) \tag{3.40}$$

As long as the vessel has a relative velocity to the water, there will be a resistance force acting in the negative x-direction hence $F_x < 0$. To isolate the added resistance due to ϕ, θ and ψ, is a straight-ahead simulation with V=3m/s $\phi = 0$, $\theta = 0$ and $\psi = 0$ conducted, and the total resistance R_T and the total resistance coefficient C_T is obtained. When calculating $C_{F_x}(\theta)$, $C_{F_x}(\theta)$ and $C_{F_x}(\theta)$ is R_T from the straight-ahead condition subtracted from F_x and subsequently C_T is added to the coefficients when F_x is calculated. For a given value of ϕ, θ and ψ is the resistance therefore expressed by equation (3.41).

$$F_x = \frac{1}{2}\rho V^2 S(C_T + C_{F_x}(\phi) + C_{F_x}(\theta) + C_{F_x}(\psi)) \tag{3.41}$$

A flow chart presenting the structure of the VPP program is visualised in figure 3.16.

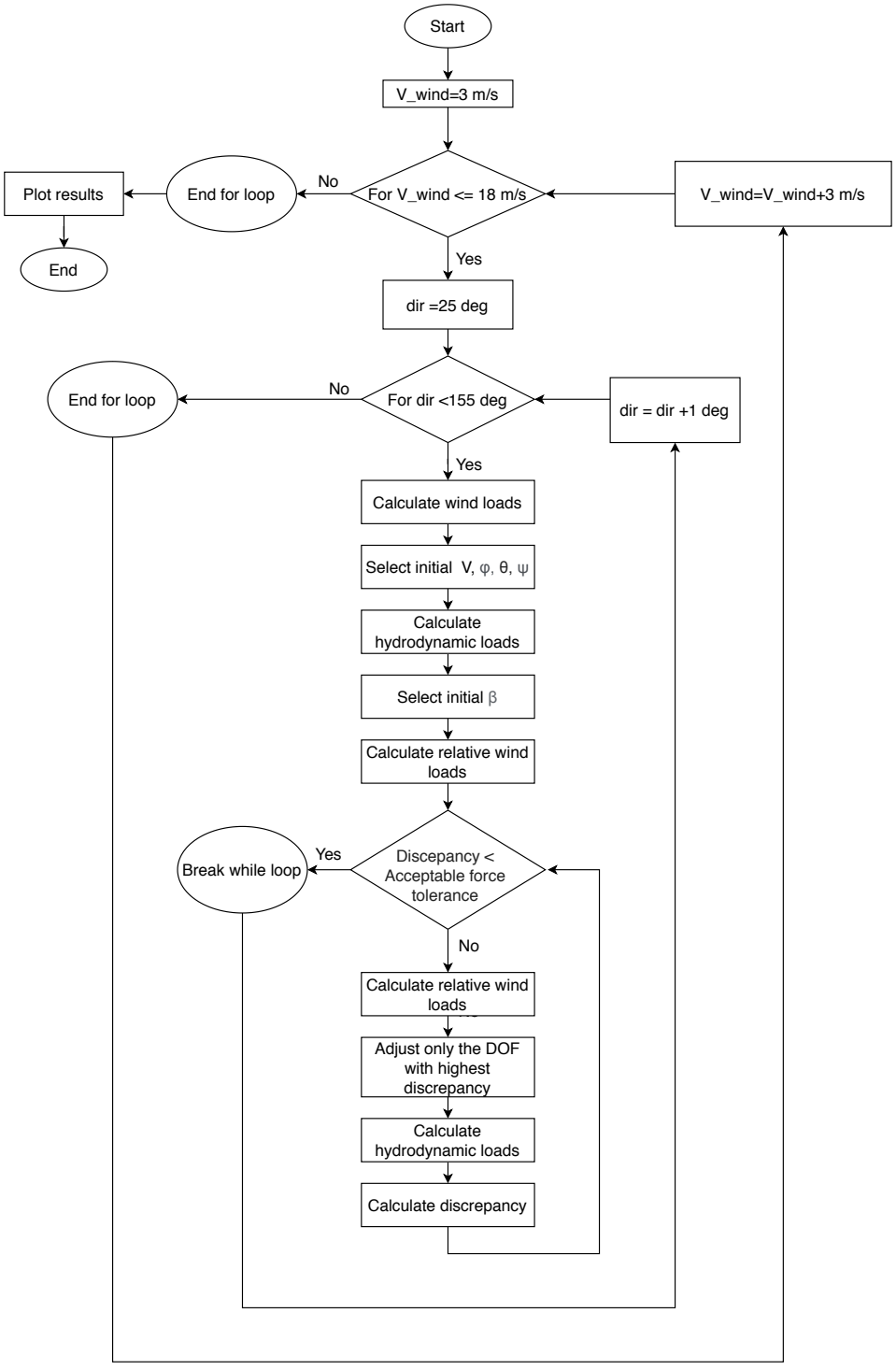

Figure 3.16: Flow chart of the VPP.

Chapter 4

Validation

4.1 Michell's thin ship theory

The validation of Michell's thin ship theory is a comparison to the results produced by Tuck and Lazauskas 1998, who studied several multihull configurations for minimising wave resistance with Michell's thin ship theory. One of the configurations examined is a Wigley hull catamaran, and its wave resistance is presented in figure 4.1. The figure also shows the wave resistance obtained with Michell's thin ship theory in the present study with the same hull.

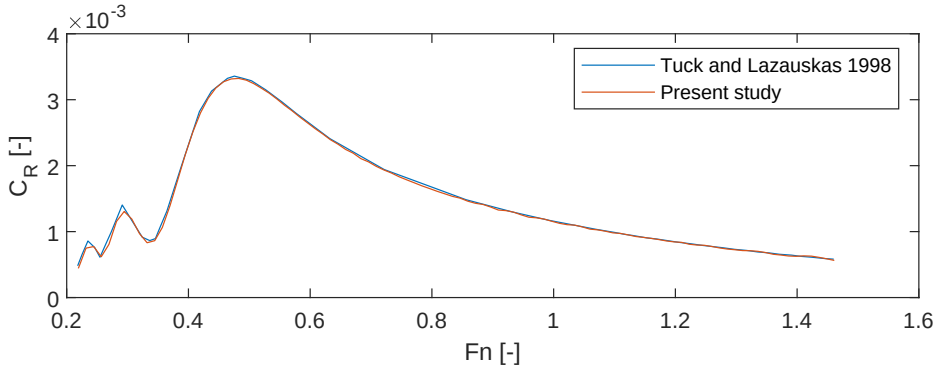

Figure 4.1: Wave resistance of a Wigley hull catamaran used to validate the code.

The curves for C_R coincide well, and it is therefore assumed the formulation of Michell's thin ship theory is correctly written in the present study.

4.2 Particle Swarm Optimisation

The PSO algorithm is validated by checking its ability to optimise a known problem in a satisfactory manner. The selected problem is detecting the minimum of the Rastrigin function given by equation (4.1).

$$f(x, y) = 20 + x^2 + y^2 - 10(cos(2\pi x) + cos(2\pi y)) \tag{4.1}$$

For -5.12<x<5.12 and -5.12<y<5.12, the Rastgrin function has 121 local minimum and one global minimum at origo. If the algorithm gets stuck on a local minimum and does not manage to detect the global minimum, it is an indication of either a bug in the program or a poor decision of the constants w, c1 and c2 in equation (3.26).

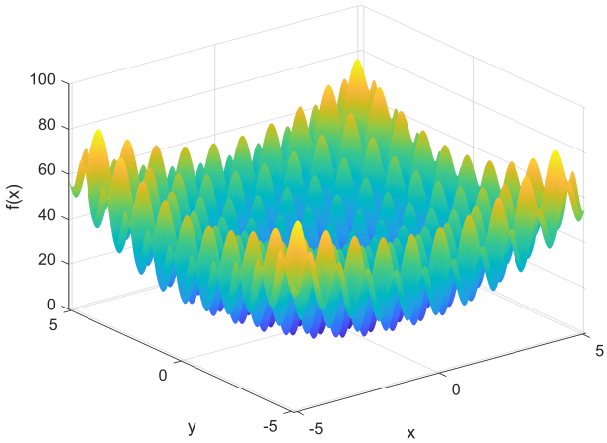

Figure 4.2: Rastrigin function

Two tests are carried out with ten identical runs each. The grid is discretised to 10 000 elements in both x and z-direction, adding up to $1 \cdot 10^8$ unique positions. In the first test is the swarm size 200, i.e. larger than the number of minimums and the number of iteration is 50. In the second test is the swarm size set to 10, it is highly likely that no particle will initially be positioned in the global minimum for at least one of the runs.

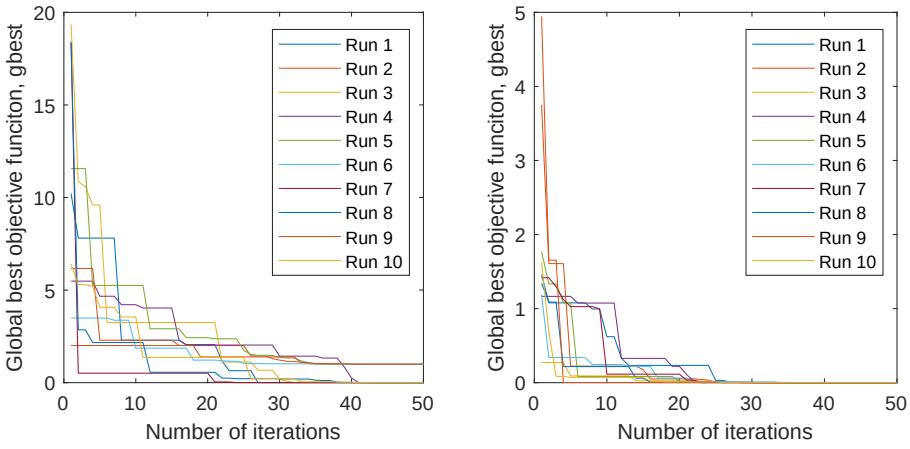

(a) Swarm size 10

(b) Swarm size 200

Figure 4.3: Twenty separate test runs of the Rastrigin function with two different swarm sizes.

Unsurprisingly, are the initial $gbest$ higher for swarm size 10 than 200 as well as the iterations needed to find the global minimum. While every run with swarm size 200 manages to locate the global minimum with less than 30 iterations, four of the runs at swarm size 10 was stuck at a local minimum after 50 iterations. Due to the convergence towards the global minimum in the majority of the test cases, it is assumed that the PSO-algorithm is formulated correctly.

4.3 Resistance models

Before the transom sterns were put aside and the towing tests were still scheduled, four geometries were obtained from optimisation and subsequently simulated with CFD. In figure 4.4 to figure 4.8 that corresponds to simulation C, D, F, and G. A is a single side hull taken from F, and B is the geometry from G but with a velocity of 2m/s. Simulations E, H, I, and J has pointy sterns. Due to restrictions in the towing tank, it was advised to reduce the displacement of the vessel to 100 kg for the model tests; hence simulation B-G has 100kg displacement, and H-J has 200kg displacement, and A has 40kg displacement. The net resistance is thus not directly comparable to the final design in the next section. All of the simulations A-J differ from the final optimisation since they have a non-zero position of the keel and torpedo, the length restriction is varied, and the stability constraint is looser. Figures showing the for simulation A to J are presented in appendix chapter A

It is not intended to compare the simulations against each other but rather to look at the difference between the resistance models and the CFD simulations. In figure 4.4 is the viscous resistance plotted for five different approaches. The first approach is CFD simulations and contains only the frictional resistance and not the viscous pressure resistance. The next two approaches utilise the ITTC'57 line in combination with each of the respec-

tive form factor. The two last approaches use ITTC'57 to determine C_F for the side hulls and the 1/7th power law and Schultz-Grunov line to determine C_F for the torpedo and keel.

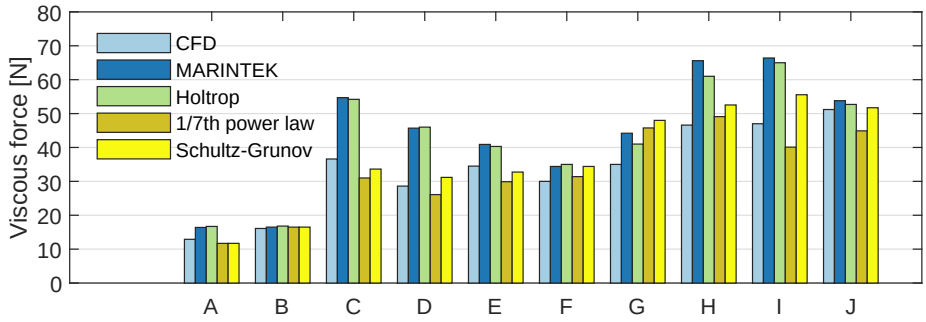

Figure 4.4: Viscous forces obtained with different methods. CFD is retrieved from simulations, MARINTEK with ITTC57 and MARINTEK form factor, Holtrop with ITTC57 and Holtrop form factor, 1/7 power law with ITTC57 for side hulls and 1/7th power law for keel and torpedo

The difference in viscous resistance between the two form factors is below 2.1% for every case except for simulation G and H, where the difference is 7.0% and 7.2%. In both cases is the viscous resistance over predicted compared to CFD by a significant amount, for example, the greatest percentage difference is simulation D, where MARINTEK is 59% greater than CFD. The percentage difference between MARINTEK and CFD for all simulations are provided in figure 4.7.

The 1/7th law and Schultz-Grunov line is performing better at some validation cases and worse at others. It is therefore a possibility that the ITTC 57' line is not the most applicable line, however it was not enough time in this project to investigate which of the frictional coefficient lines that performs best.

It is believed that the main contribution to the discrepancy is the deformation of the free surface along the hull, that leads to a reduction in the wet area in the simulations while this effect is not captured with the models in figure 4.4.

For the optimised geometry in the result chapter, the wet surface from CFD is 12.7% less than in still water. Integrating ρ over the hull with a threshold of $\rho > 10kg/m^3$ resulted in 4038.5 kg/m which is 96.3% of the still water values. Hence, the deformation of the free surface has a noticeable effect on the wet area. If equation (3.5) is solved for $(1+k)C_F$ with S being 96.3% of the original wet area and R_F is obtained from CFD the output becomes $2.53 \cdot 10^{-3}$. The deformation of the free surface is displayed in figure 4.5.

Another possible reason is the friction resistance obtained from CFD excludes the viscous pressure. However, that effect is nearly removed in the resistance models if the form factor is omitted. The scatter plot in figure 3.5 indicates that the form factor obtained from MARINTEK seldom exceed 0.06 ergo will not over-predict more than 6% of the viscous resistance.

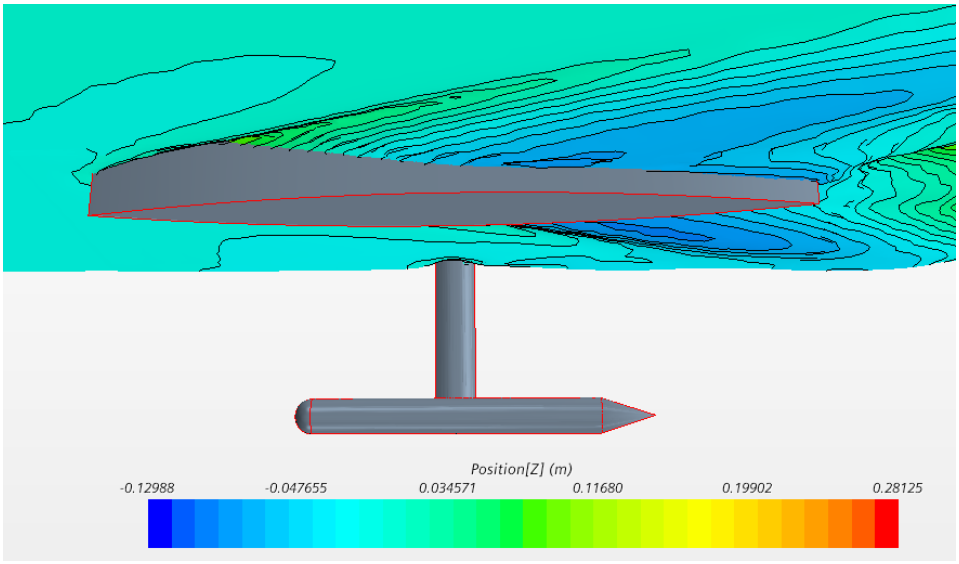

Figure 4.5: Deformation of the free surface at 3m/s

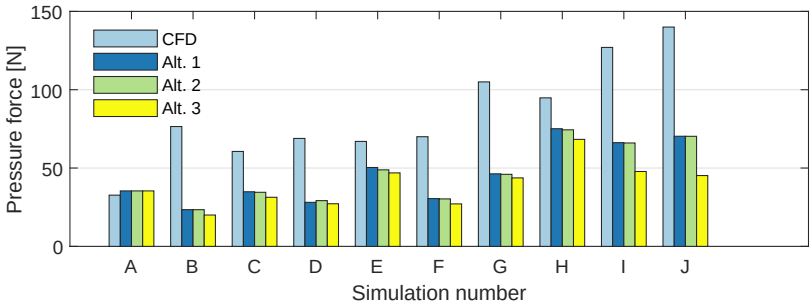

Figure 4.6: Comparison in pressure resistance between CFD and the three alternative combinations; Alt. 1, Alt. 2 and Alt. 3.

In figure 4.6 is four different methods compared, where the first is CFD simulations, and the three alternatives are different combinations of resistance models based on potential theory and regression formula. Alternative 1 use the wave resistance formula in equation (3.11), equation (3.12), and equation (3.13) for the side hulls and the keel with the regression formula in equation (3.16) for the torpedo. Alternative 2 differ from alternative 1 by applying Michell's thin ship theory to the side hulls and keel separately and then adding the resistance together at the end. Alternative 3 differ from alternative 1 by utilising equation (3.14) to determine the wave resistance of the torpedo instead of equation (3.16).

Similar to the viscous resistance is the deformation of the free surface affecting the pres-

Alternative	Side hulls and keel	Torpedo
1	equation (3.11), equation (3.12), and equation (3.13)	equation (3.16)
2	equation (3.11) and equation (3.12) separately for each hull part	equation (3.16)
3	equation (3.11), equation (3.12), and equation (3.13)	equation (3.14)

Table 4.1: Resistance models used for the three alternatives in figure 4.6.

sure resistance too. In all of the simulations is a wave crest present in the bow and a wave trough present at the stern. The net hydrostatic pressure will, therefore, act in the opposite direction of the movement. The magnitude of this effect can be found by integrating the hydrostatic pressure on the hull surface. However, this is not done since the built-in field function for hydrostatic pressure was not able to obtain a result. It was attempted to find it with a user-defined field function, but difficulties were encountered since the hydrostatic pressure in one cell is dependent on the density of the cells above it.

In figure 4.7 is the resistance obtained from the methods in table 3.1 compared to the resistance obtained from CFD simulations. That corresponds to the difference between MARINTEK and CFD in figure 4.4 and Alt.1 and CFD in figure 4.6. The discrepancy for pressure resistance is given as the difference between CFD and Alt. 1 and then divided by the magnitude of CFD, and similarly for viscous resistance and total resistance.

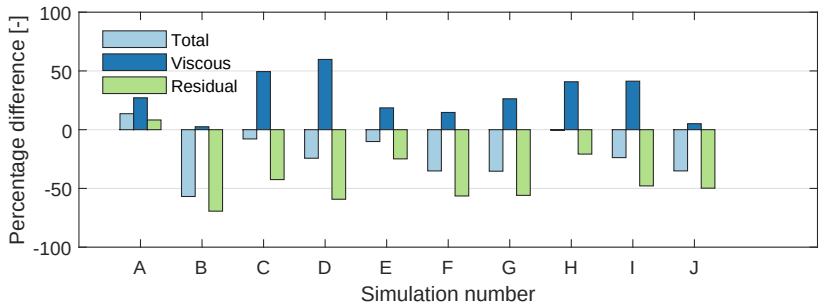

Figure 4.7: The percentage difference between the resistance obtained from CFD and the resistance models in table 3.1

The methods in table 3.1 generally over-predict viscous resistance and underestimate pressure resistance. Hence the difference in total resistance is usually reduced due to a cancellation between the two. The difference in both viscous and pressure resistance is highly varying and exceeds 50% in some of the simulations.

In figure 4.8 is the total resistance presented for the CFD simulations and the methods in table 3.1.

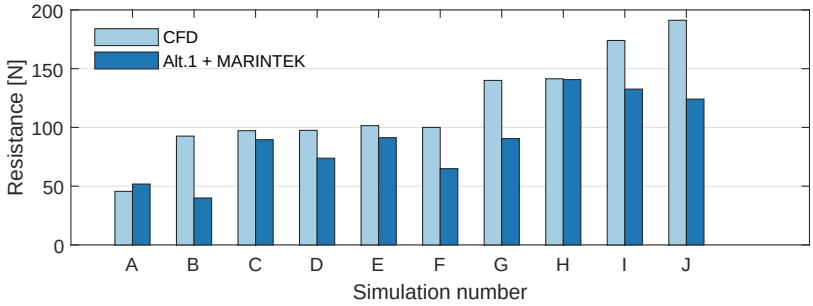

Figure 4.8: The total resistance compared between the CFD results and the resistance models in table 3.1(Denoted Alt.1 + MARINTEK)

Chapter 5

Results

5.1 Optimisation

The optimisation program is executed six times with 200 swarm size and 10 iterations. The geometry with corresponding resistance from each run is presented in section 5.1. A fairly small spread is observed for the resistance, with five out of six runs differing only by two newton. Both the length and the breadth are consistent for every run, and they are both at the upper limit of the range in table 3.4. The breadth of the side hull is almost consistent, with only 0.02m difference between the lowest and highest value. The length of the keel is at the lower boundary of acceptable values for the five runs with lowest resistance. The breadth of the keel is also on or close to the lower limit of acceptable values. The height of the keel is different in every run, with the majority being between 0.31m and 0.38m. The length of the torpedo is also varying, and the five best cases ranging from 1.67m to 1.80m.

Optimisation run	1	2	3	4	5	6
L	3.00 m	3.00 m	3.00 m	3.00 m	3.00 m	3.00 m
B Vessel	2.50 m	2.50 m	2.50 m	2.50 m	2.50 m	2.50 m
B SH	0.37 m	0.37 m	0.37 m	0.39 m	0.39 m	0.37 m
L keel	0.20 m	0.20 m	0.20 m	0.20 m	0.20 m	0.43 m
B Keel	0.06 m	0.05 m	0.05 m	0.05 m	0.09 m	0.05 m
H Keel	0.51 m	0.38 m	0.31 m	0.33 m	0.36 m	0.08 m
L torp	1.80 m	1.72 m	1.72 m	1.67 m	1.67 m	1.36 m
Resistance	132 N	132 N	132 N	134 N	134 N	137 N

Optimisation run 1 from section 5.1 is selected as the desired geometry for the project. The development of the objective function, i.e. resistance, for run 1 is plotted in figure 5.1.

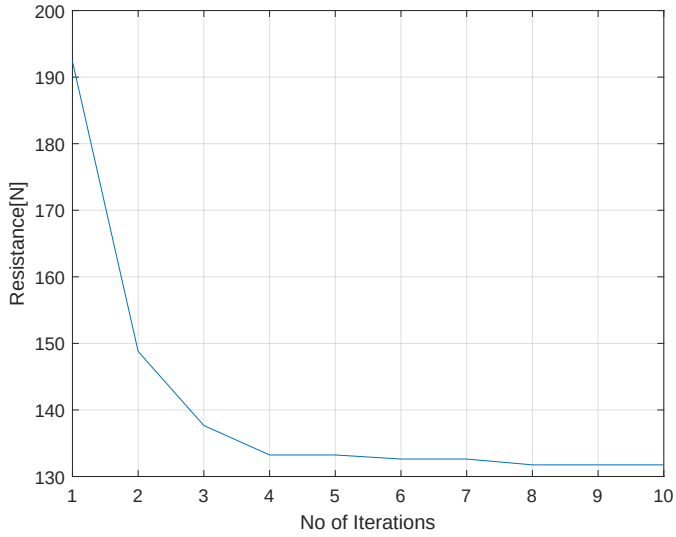

Figure 5.1: Development of objective function during the optimisation.

The lowest resistance is improved rapid in the first 4 iterations, and then converge slowly toward 132N.

The exact values of each parameter for optimisation run 1 is presented in table 5.1. In addition to the seven optimisation parameters are also the length of the torpedo and the height of the side hulls included.

Variabel	Size
L Side hull	3.000 m
B Vessel	2.500 m
B Side hull	0.374 m
L Keel	0.200 m
B Keel	0.062 m
H Keel	0.512 m
D Torpedo	0.1769 m
L Torpedo	1.769 m
H Side hull	0.5860 m
Centre of gravity above keel	0.63

Table 5.1: Geometical variables obtained from optimisation

A resistance plot is presented in figure 5.2, where curves are established by the resistance models in table 3.1 and the scatter plot is obtained by CFD.

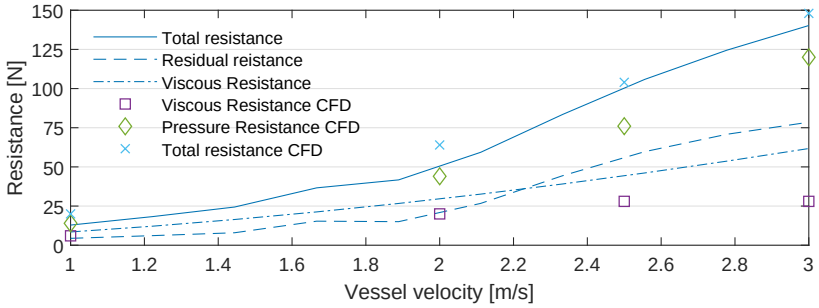

Figure 5.2: Resistance plot obtained from the resistance models in table 3.1 and CFD

The residual resistance coefficient for the vessel is plotted in figure 5.3. As anticipated by Graff, Kracht, and G. Weinblum 1964 is the maximum residual resistance coefficient positioned close to Froude number 0.45. What is more uncommon is the sudden increase in C_R at Froude number 0.1. This can be explained by the Froude number in figure 5.3 is calculated with the length of the side hulls, and the ratio of Froude number between the side hulls and the keel is $\sqrt{L_{pp}/L_{Keel}}$. Hence, when the Froude number of the vessel is 0.1 is the Froude number of the keel 0.39.

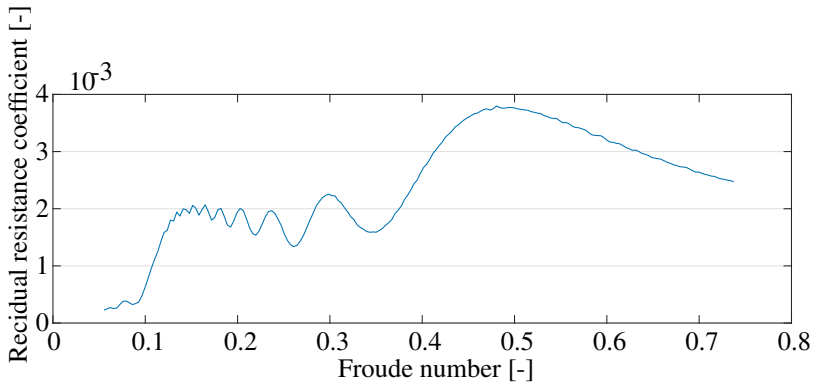

Figure 5.3: Residual resistance coefficient

5.2 CFD

A complete list of simulations executed with CFD is presented in table 5.2. The four columns to the left express the input value of each DOF, while the five columns to the right show the resulting loads in each directions. It should be emphasised that the coordinate system is fixed to the vessel and not the direction of travel.

In the first simulation is the orientation equal to zero in all direction and the velocity is 3m/s. The following seven simulation keep 3m/s but a rotation in one of the DOF is introduced. As stated in chapter 3 is the connection between ϕ and M_x greatly dependent on hydrostatics. Thus, additional simulations with zero velocity is conducted to separate the hydro static loads from the hydro dynamic loads. Due to limited time, it is not conducted any simulations to separate $C_{M_y}(\theta)$ and $C_{M_y,0}(\theta)$

It is observed that F_x is 148N when the vessel is aligned with the free stream, and the force increases with a change in all of the three angles. Of the seven different angles, does the negative θ result in the lowest F_x. F_y is strongly influenced by ψ and almost invariant of ϕ and θ. M_x is mainly dependent on θ but has a small contribution from ψ and no contribution from θ. M_y seems to be influenced by all the DOFs but the most prominent is θ. M_z is mostly dependent on ψ but has an evident contribution from θ as well.

Table 5.2: CFD simulations

Sim #	ϕ[°]	θ[°]	ψ[°]	V[m/s]	F_x[N]	F_y[N]	M_x[Nm]	M_y[Nm]	M_z[Nm]
1	0	0	0	3	-148	0	0	-84	0
2	2	0	0	3	-179	-2	-704	-66	-56
3	4	0	0	3	-186	-3	-1390	-63	-113
4	0	-2	0	3	-166	0	0	64	0
5	0	2	0	3	-190	0	0	-212	0
6	0	0	2	3	-178	122	-14	-97	104
7	0	0	4	3	-198	267	60	-95	199
8	0	0	6	3	-226	392	66	-74	317
9	0	-2	0	0	0	0	0	226	0
10	0	0	0	0	0	0	0	30	0
11	0	2	0	0	0	0	0	-210	0

Due to symmetry is it only necessary to investigate either positive or negative angles in both roll and yaw. In section 5.2 is the coefficients of negative ϕ and ψ therefore copied from the positive angles, and the sign is changed where it is suitable. The sign of the coefficients is in accordance with the axis in figure 3.14. Hence, the negative C_T does not imply a negative total resistance, but a resistance force acting in the negative x-direction.

	Angle						
	-6	-4	-2	0	2	4	6
C_T				-0.0394			
$C_{Fx}(\phi)$		-0.0101	-0.0082		-0.0082	-0.0101	
$C_{Fx}(\theta)$			-0.0048		-0.0112		
$C_{Fx}(\psi)$	-0.0207	-0.0133	-0.0080		-0.0080	-0.0133	-0.0207
$C_{Fy}(\phi)$		0.0003	0.0002		-0.0002	-0.0003	
$C_{Fy}(\psi)$	-0.1042	-0.0710	-0.0324		0.0324	0.0710	0.1042
$C_{Mx}(\psi)$	-0.0173	-0.0160	0.0037		-0.0037	0.0160	0.0173
$C_{My}(\phi)$		0.0056	0.0048		0.0048	0.0056	
$C_{My}(\theta)$			0.0431	-0.0303	-0.0431		
$C_{My}(\psi)$	0.0239	-0.0263	-0.0311		-0.0311	-0.0263	0.0239
$C_{Mz}(\phi)$		0.0300	0.0149		-0.0149	-0.0300	
$C_{Mz}(\psi)$	-0.0843	-0.0529	-0.0277		0.0277	0.0529	0.0843
$C_{Mx,0}(\phi)$		3.3267	1.6849		-1.6849	-3.3267	
$C_{My,0}(\theta)$			0.5409	0.0718	-0.5026		

The surface elevation for a rotation in each degree of freedom is presented in figure 5.4. The kelvin wave system with transverse and divergence waves are evident in all four cases. The wave amplitude in figure 5.4a, when the vessel has a positive yaw angle, is greater on starboard side than port side. The wave system in figure 5.4b and figure 5.4d is similar, although the wave amplitude is smaller in trim than with zero rotation. In the roll condition in figure 5.4c is nearly all wave making provided by the starboard side hull hence the wave system is similar to the wave system of a mnohull.

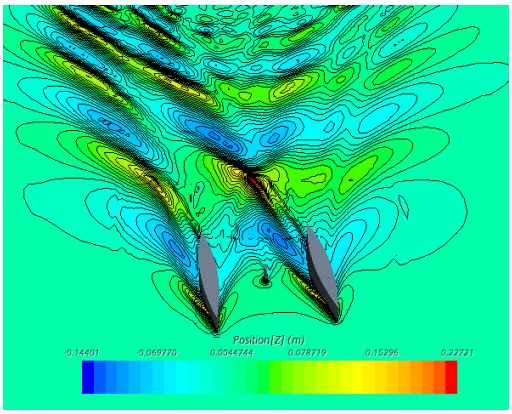

(a) Sim 8 (ψ=6°)

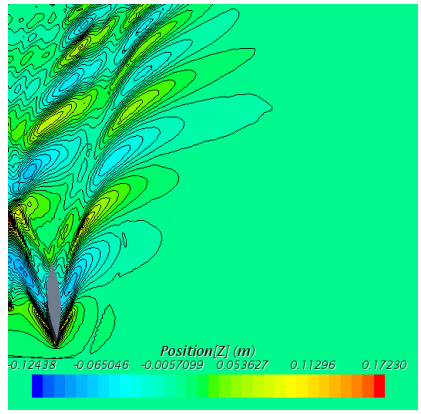

(b) Sim 5 (θ=2°)

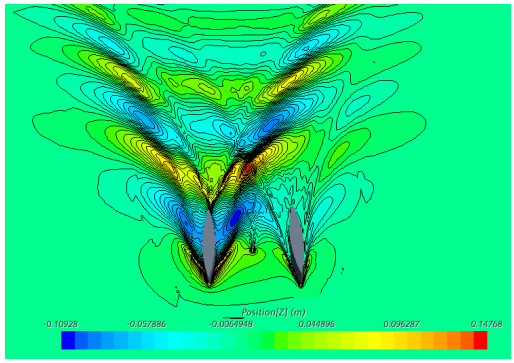

(c) Sim 3 (ϕ=4°)

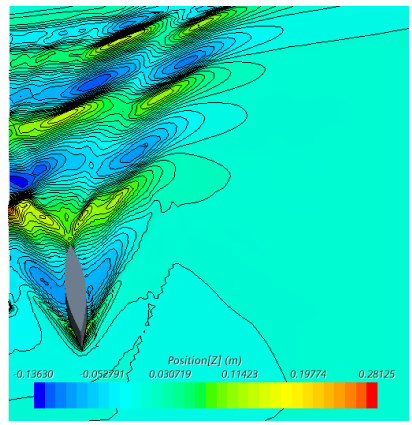

(d) Sim 1 (ϕ=θ=ψ=0°)

Figure 5.4: Surface elevation for yaw, trim, roll and no rotation.

5.3 VPP

Six different wind velocities are evaluated with the VPP. The corresponding vessel velocity is then plotted as a function of true wind direction in figure 5.5. The largest velocities are obtained at ≈90° true wind direction for low wind speeds and ≈110° true wind direction at the higher wind speeds. According to the VPP is the vessel capable of obtaining a velocity up to 1m/s at 3m/s true wind speed, and 1.8m/s at 6m/s wind speed, and 2.5m/s at 9m/s true wind speed. The highest velocity made good is observed for 42° wind direction for nearly all velocities.

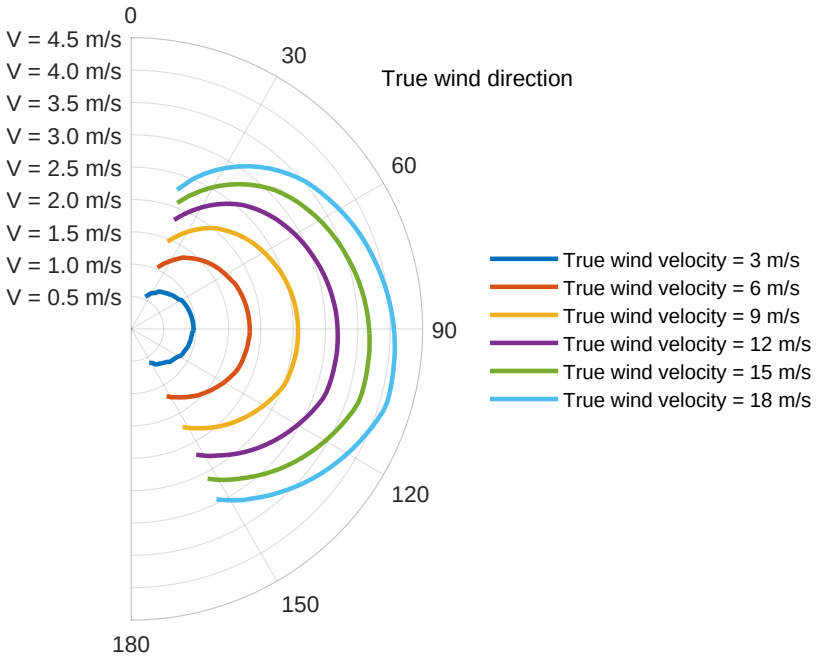

Figure 5.5: Vessel speed as a function of true wind direction for various true wind speeds.

The orientation of the vessel at 9m/s wind velocity is plotted in figure 5.6. The roll angle is negative for low wind angles, cross zero at about 110°, and is positive for larger wind angles. The trim angle is positive for all wind directions and reach a maximum at about 80°. Similar to the roll angle, is the yaw angle negative below 110° and positive above, but the magnitude is substantially higher than the roll angle.

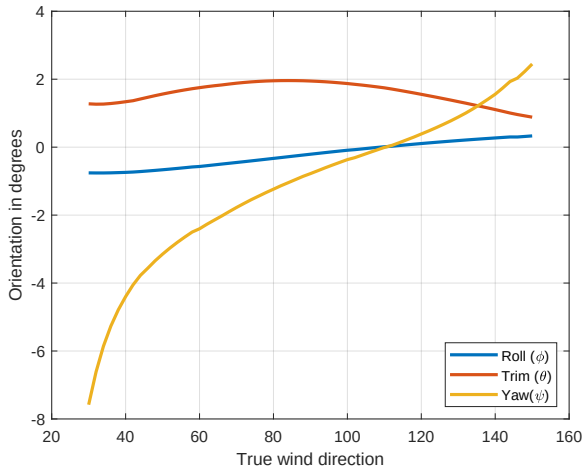

Figure 5.6: Orientation of the vessel as a function of true wind direction for 9m/s wind velocity.

The added resistance due to the orientation in figure 5.6 is plotted in figure 5.7. The line denoted straight ahead is the contribution to the resistance from the total resistance coefficient. The roll angle result in the least resistance and has a maximum contribution of 5N, and is zero at 110°. The resistance due to trim is low for both small and large angles and maximum of 30N at about 90°. The yaw angle produce most resistance for small and large wind angles with a maximum of 24N at 30°, and is zero at 110°. The maximum resistance from the total resistance coefficient is 110N at 90°.

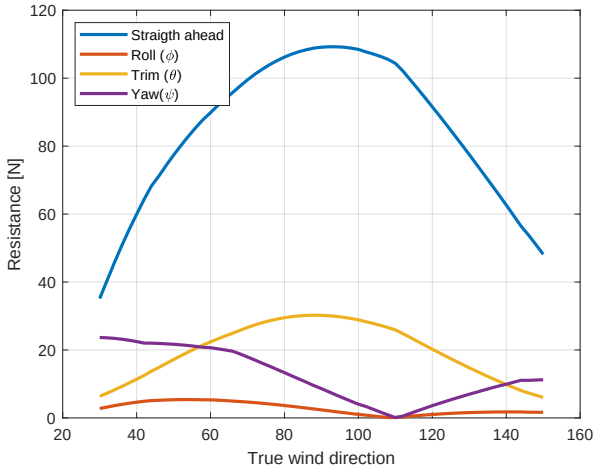

Figure 5.7: Added resistance arising from the different DOFs as a function of true wind direction at 9m/s wind velocity

Chapter 6

Discussion

The resistance curve in figure 5.2 is consistent with the observations in the validation chapter. The results show a great discrepancy in the resistance obtained from potential theory and empirical formulas compared to the resistance obtained from CFD simulations. Hence, either Michell's thin ship theory accompanied with empirical formulas result in a poor prediction of the resistance or the CFD simulations are conducted in an unsatisfactory manner, or they may be both erroneously. The resistance curves show that the discrepancy is also present at lower velocities than the 3 m/s tested in the validation chapter. The reason for the discrepancy is argued for in the validation chapter and, the main reason is believed to be the deformation of the free surface.

It is observed that changing the vessel orientation in any direction result in increased resistance. It was expected that a negative trim angle would lift the vessel slightly higher in comparison to the straight-ahead condition and accordingly reduce the resistance. However, it is observed that a negative trim angle produce more resistance than the straight-ahead condition.

The simulations in table 5.2 that form the basis of the VPP program does not contain any simulations where two or more degrees of freedom are non zero at the same time, and this presents a limitation to the VPP. For instance, if the yaw angle is non-zero, and the trim angle is increased from zero to a positive angle, the yaw moment will increase as well. In the present work, however, it is assumed that the yaw moment is unaffected by the trim angle. This simplification is only valid when the yaw angle is equal to zero due to symmetry.

The simulations in table 5.2 contain a bare minimum of the necessary conditions needed to construct a VPP. The plot in figure 5.5 evaluates wind velocities up to 18m/s, which involve yaw and trim angles up to 8°. However, the simulations only cover trim angles of $\pm 2^\circ$ and yaw angle up to 6°. The roll angle on the contrary never exceeds 2.5°, and the simulations include 2° and 4°.

The only non-zero velocities in table 5.2 is 3m/s and the coefficients in section 5.2 is made dimensionless by dividing with the squared velocity. It is no guarantee and probably incorrect that the coefficients are independent of the velocity. Additional simulations, for instance at 1m/s and 2m/s, would reduce this error and is advised for further work.

According to the VPP is the velocity of the vessel more than 2 knots at a gentle breeze and more than 4 knots at moderate breeze if the wind is reaching. This is comparable to the Saildrone in the literature review, who has specified average velocity of 2-3 knots and a top speed above 8 knots. The smaller Sailbouy vessel recorded an average velocity of 0.55m/s with 6m/s wind speed, according to the VPP will the vessel in this study obtain a velocity between 1.5m/s and 2m/s with the same wind conditions.

According to Harstveit 2005 is the 50% percentile of wind velocity in the north sea approximately 9m/s. With all simplifications and assumptions aside, that means the vessel can obtain a velocity of 2.5m/s more than 50% of the time. However, the neglected added resistance in waves and air resistance will reduce the velocity of the vessel. Additionally, during storms will the sail seek to avoid large forces hence the 50% percentile of operable wind speeds will be somewhat lower. If the vessel is not beam reaching the velocity will be reduced according to figure 5.5.

Although the moment M_x is predominantly dependent on the roll angle, is it also dependent on the yaw angle. Since a positive yaw angle implies a positive y-force on the torpedo and keel, is it expected to see a positive M_x. This is true for 4° and 6° yaw angle, but it comes as a surprise that 2° yaw angle results in negative M_x.

As expected will the vessel always have a positive trim angle since the lift from the sail act in the positive x-direction. Also, the trim angle peaks at around 80° since the lift acts almost straight ahead and the relative velocity of the wind is larger at beating than broad-reaching. The roll and yaw angles are zero at approximately 110° since the relative wind direction is slightly above 90° and the y-component of the lift force and drag force is equalised. For relative wind direction less than 90° does the lift force act in the positive y-direction hence the yaw and roll is negative. Further, when the relative wind direction exceeds 90° does the y-component of the lift change sign, and as a consequence will roll and yaw change sign as well.

The added resistance plot in figure 5.7 show good coherence with the orientation plot in figure 5.6. In general, the larger the absolute value of roll, trim and yaw angles, the larger the added resistance becomes. The added resistance due to roll is minor compared to yaw and trim. At maximum VMG , i.e. 42°, is yaw the most significant contribution to the resistance. At beam-reach is the resistance due to trim dominant, and for the larger wind velocities in chapter C is the resistance due to trim tremendous. The significant trim resistance at high velocities should not be taken on trust since the trim angle exceeds the simulated angles with CFD.

To reduce the resistance introduced by the trim angle, it was considered to optimise the position of the torpedo and the keel. It is expected that shifting them forward will reduce the resistance since this will counteract the trim moment from the sail. However, implementing the change in resistance due to their position complicates the optimisation for

many reasons. The regression formula for the wave resistance of the torpedo would have one more unknown, the desired trim moment induced by the sail needs to be determined, or several moments will have to be evaluated. Additionally, the optimisation process must include a balance of the hydrodynamic moment and the sail moment.

Future work

The discrepancy in the predicted resistance is the most compelling topic to investigate in future work. The preferable approach is to conduct towing tests and see which of the methods that is furthest away from reality.

Another topic for future work is the further development of the VPP. Among the simulations of interest are trim and yaw angles up to 8°, different velocities at the same vessel orientation, combined rotation in two or three directions, and straight-ahead condition with a propeller.

Throughout the entire thesis is the centre of gravity in the same position. Changing the centre of gravity will affect the stability of the vessel and subsequently, the change in resistance due to the vessel orientation. Investigating the magnitude of this effect would be helpful when deciding building materials, batteries and payload position.

The propeller design is not examined in this thesis but is an exciting topic for future work. For example, how much thrust can be produced when the wind is absent and for how long time, also how much energy can be generated at different wind speeds. The optimum balance on how much of the thrust produced by the sail is used to generate power and how much is kept untouched.

The added resistance in waves is neglected, although it is highly likely that the vessel will travel in sea states where this resistance contributes greatly to the total resistance. It will enhance the VPP if the added resistance in waves is incorporated in the resistance prediction.

The manoeuvrability of the vessel will be significantly reduced when the vessel has a positive trim angle, due to the decreased draught of the rudders. The problem will be reduced if the torpedo and keel are shifted forward, however, modifications of the rudder may be necessary or even installed to the torpedo instead of the side hulls.

The stability of the vessel and especially the self-righting ability is essential and is barely discussed in this thesis.

Chapter 7

Conclusion

This research has investigated the possibility of using simple geometrical shapes to design a USV. The design consist of two side hulls and a keel with constant water plane sections, and a torpedo consisting of a half dome, a cylinder and a cone. The advantage of this design is a great ability to withstand roll moments compared to monohulls, the large deck area can be fitted with many solar panels, the torpedo enables censoring below the water surface.

The approach was to reduce the resistance of the vessel by optimising the dimensions of each hull element. Due to the unconventional hull shape, a combination of different resistance models is utilised to take care of the different resistance components for every part. These methods over predict the viscous resistance and underpredict the wave resistance compared to results from CFD simulations. It is presumed that the CFD simulations are more credible as they account for the deformation of the free surface. It is assumed that the outcome of the optimisation is a hull close to the least possible resistance, for the given hull shape, constraints and resistance models.

The VPP is based on too few data points to get a detailed prediction of the vessel's performance. Still, it is assumed to give a sufficient indication of the velocities that can be expected at various wind conditions. The predicted velocity of the vessel is of similar magnitude as the Saildrone, and slightly faster than the smaller Sailbuoy.

Based on the results from the VPP is it a promising design, but it needs further evaluation specified in the future work section.

Bibliography

Cairoli, Claudio (2002). Analysis of the IMS Velocity Prediction Program, p. 61.

Doctors, Lawrence J. and Alexander H Day (2001). Steady-State Hydrodynamics of High-Speed Vessels with a Transom Stern. en. Twenty-Third symposium on naval hydrodynamics, p. 15.

Faltinsen, Odd M (2005). Hydrodynamics of High-Speed Marine Vehicles. English. Cambrigde University Press. ISBN: 978-0-521-17873-0.

Ghani, Mahmud Hasan et al. (Sept. 2014). The SailBuoy remotely-controlled unmanned vessel: Measurements of near surface temperature, salinity and oxygen concentration in the Northern Gulf of Mexico. en. Methods in Oceanography 10, pp. 104–121. ISSN: 22111220. DOI: 10.1016/j.mio.2014.08.001. URL: https://linkinghub.elsevier.com/retrieve/pii/S2211122014000395 (visited on 06/16/2020).

Graff, W, A Kracht, and G Weinblum (1964). Some extensions of D.W. Taylor's standard series. The Society of Naval Architects and Marine Engineers. SNAME.

Harstveit, Knut (Nov. 2005). Extreme value analysis of hindcast wind data from the maritime areas surrounding Norway.

Harvald, Sv. Aa. (1983). Resistance and propulsion of ships. English. XII. Ocean Engineering. New York: Wiley. ISBN: 0-471-06353-3.

Havelock, T. H. (1931). The wave resistance of an ellipsoid. en, p. 7.

Hoerner, Sighard F. (1965). FLUID-DYNAMIC DRAG. English.

Holtrop, J (1984). A statistical re-analysis of resistance and propulsion data. en. International Shipbuilding Progress 28, pp. 272–276.

Homaifar, Abdollah, Charlene X. Qi, and Steven H. Lai (Apr. 1994). Constrained Optimization Via Genetic Algorithms. en. SIMULATION 62.4, pp. 242–253. ISSN: 0037-5497, 1741-3133. DOI: 10.1177/003754979406200405. URL: http://journals.sagepub.com/doi/10.1177/003754979406200405 (visited on 06/01/2020).

IMO (2020). Introduction to IMO. URL: http://www.imo.org/en/About/Pages/Default.aspx (visited on 05/29/2020).

ITTC (May 2011). ITTC – Recommended Procedures and Guidelines. English.

Kennedy', James and Russell Eberhart (1995). Particle Swarm Optimization. en. Proceedings of the International Conference on Neural Networks; Institute of Electrical and Electronics Engineers 4, pp. 1942–1948. DOI: 10.1109.

Michell, Mr J H (1898). The Wave-Resistance of a Ship. en. Philosophical Magazine. 5th ser. 45, pp. 106–123.

Moonesun, Mohammad et al. (2016). Optimum L/D for Submarine Shape. en. INDIAN J. MAR. SCI. 45.1, p. 6.

NOAA (2020). How are satellites used to observe the ocean? URL: https://oceanservice.noaa.gov/facts/satellites-ocean.html (visited on 05/29/2020).

Sabine, Christopher L. et al. (July 2004). The Oceanic Sink for Anthropogenic CO_2. Science 305.5682, p. 367. DOI: 10.1126/science.1097403. URL: http://science.sciencemag.org/content/305/5682/367.abstract.

Smith, Shawn R. et al. (2019). Ship-Based Contributions to Global Ocean, Weather, and Climate Observing Systems. Frontiers in Marine Science 6, p. 434. ISSN: 2296-7745. DOI: 10.3389/fmars.2019.00434. URL: https://www.frontiersin.org/article/10.3389/fmars.2019.00434.

Steen, Sverre (2014). TMR4247 Marin Teknikk 3 - Hydrodynamikk. Norwegian. Akademika forlag.

Steen, Sverre and Knut Minsaas (Nov. 2013). TMR 4220 - Naval Hydrodynamics Ship Resistance. Englsih. Akademika forlag.

Tuck, E O and L Lazauskas (June 1998). OPTIMUM HULL SPACING OF A FAMILY OF MULTIHULLS. en, p. 39.

UNESCO (2020). Monitoring the Ocean. URL: https://en.unesco.org/themes/monitoring-ocean (visited on 05/29/2020).

Veers, Jens and Bertram Volker (May 2006). Development of the USV Multi-Mission Surface Vehicle III. PROCEEDINGS OF COMPIT '06, pp. 346–355.

Weinblum, Amtsberg, and Bock (1936). Tests on Wave Resistance of Immersed Bodies of Revolution. Mitteilungen Preussische Versuchsanstalt Wasserbau Schiffbau.

Appendices

Appendix A

Validation simulations

Case A

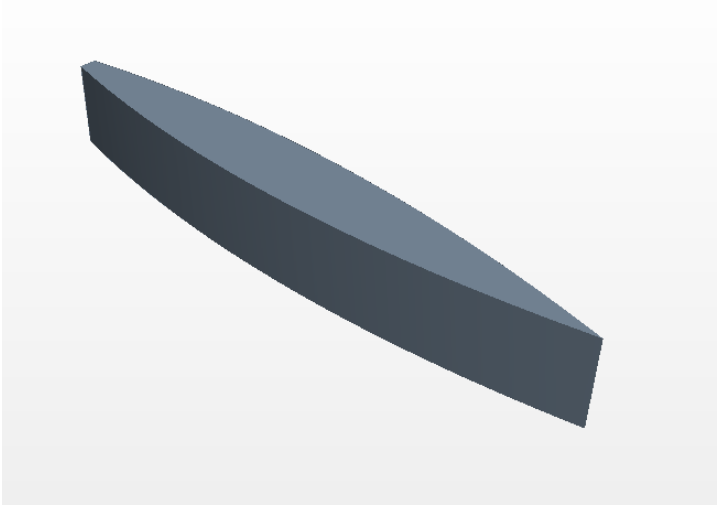

Case B & G

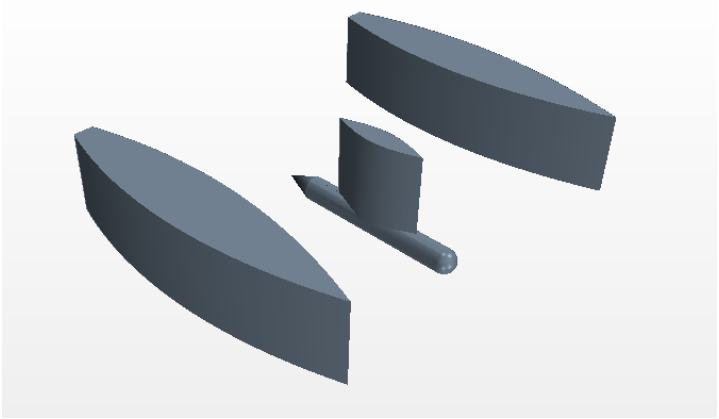

Case C

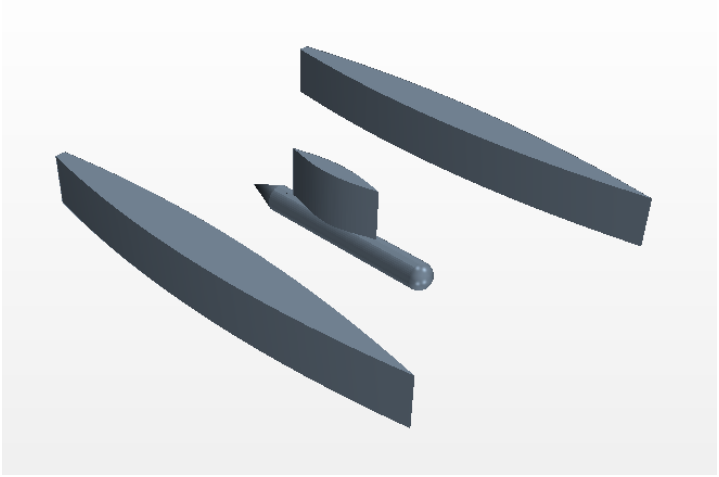

Case D

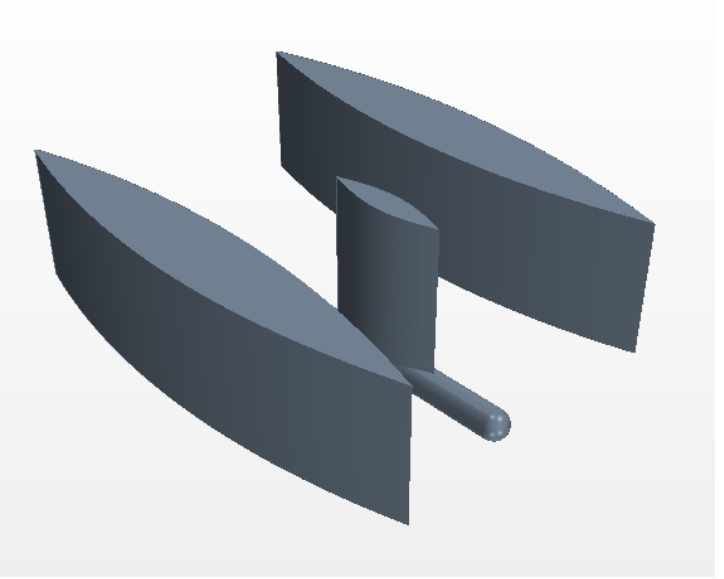

Case E

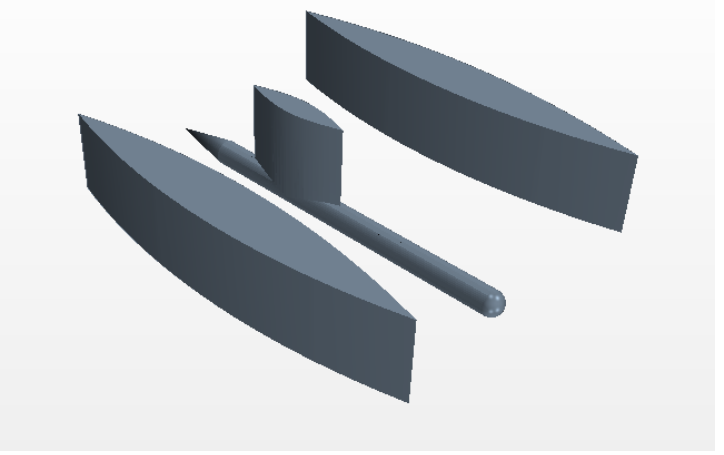

Case F

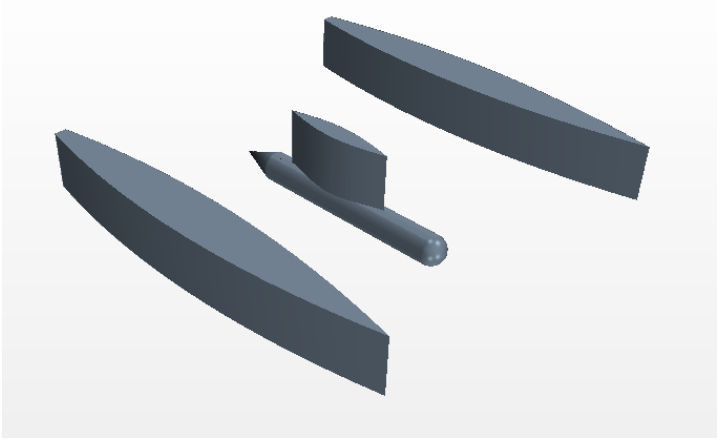

Case H

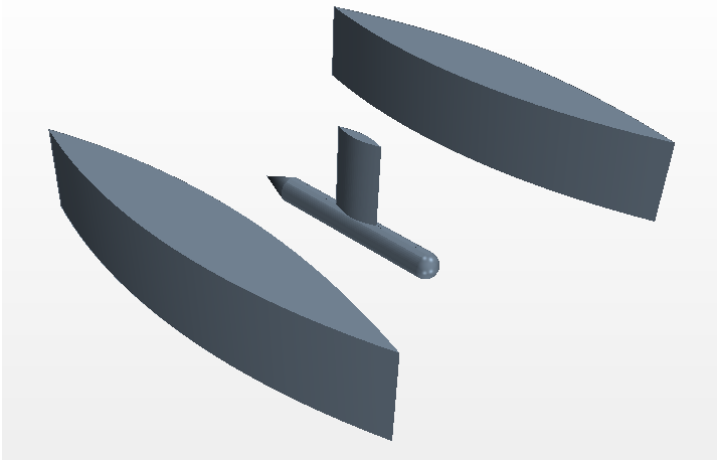

Case I

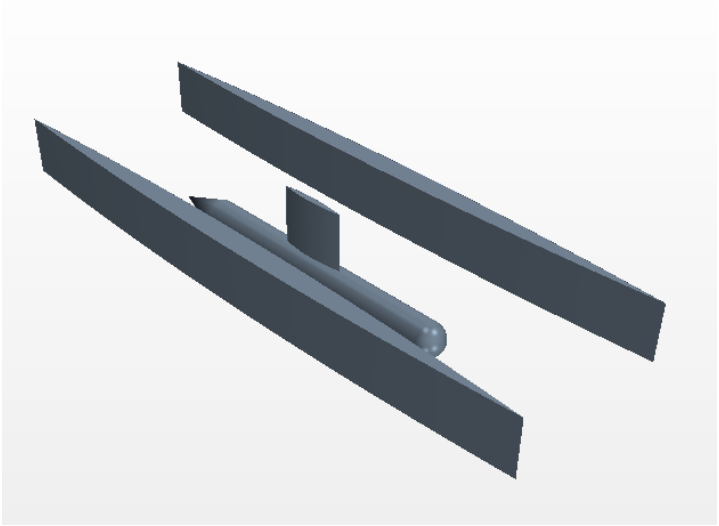

Case J

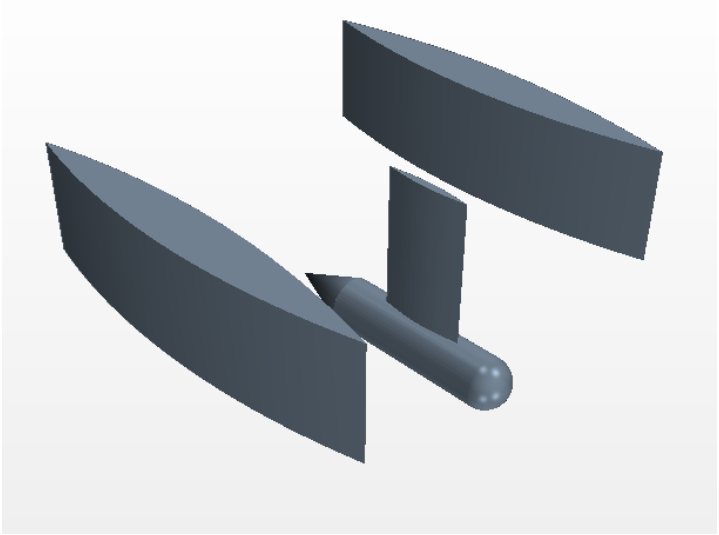

Appendix B

VPP orientation

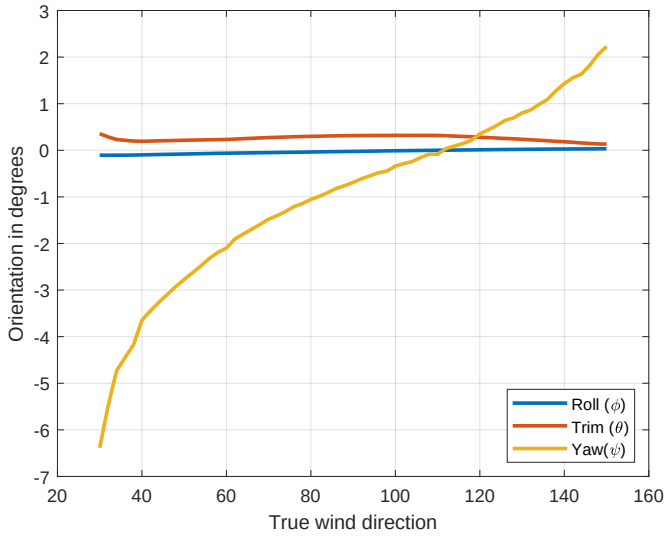

Figure B.1: Wind velocity: 3m/s

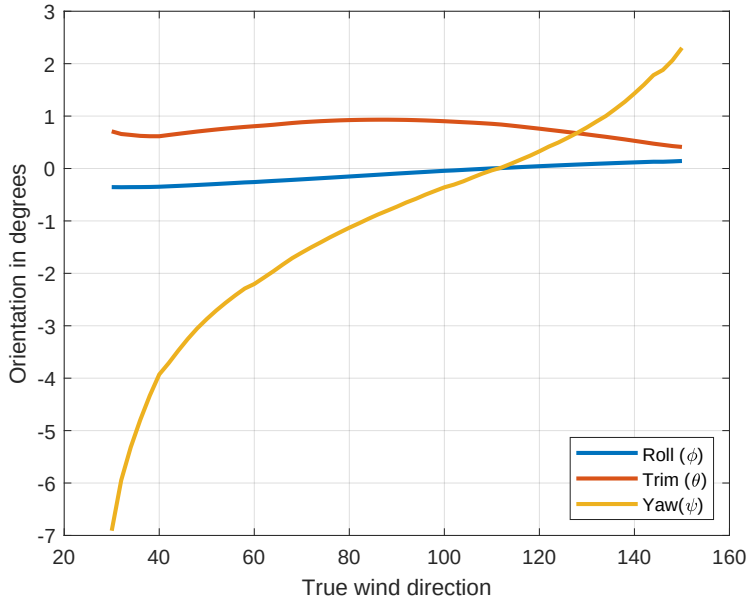

Figure B.2: Wind velocity: 6m/s

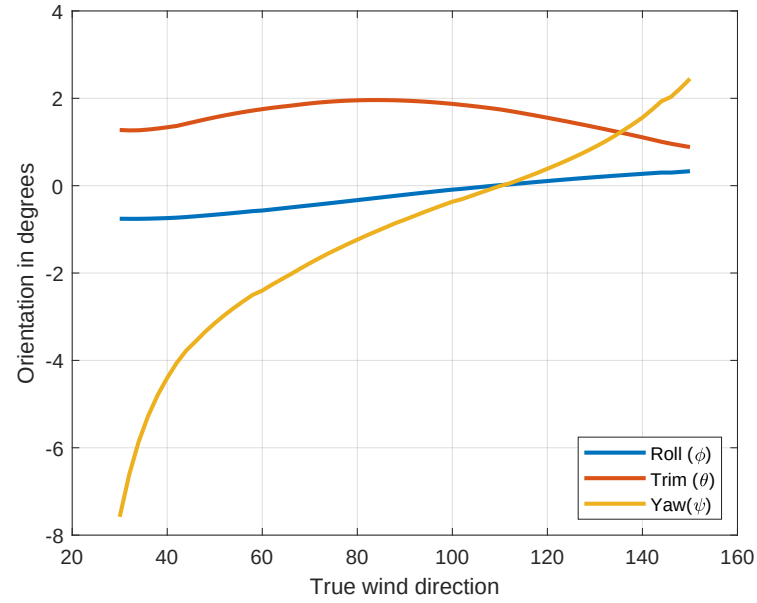

Figure B.3: Wind velocity: 9m/s

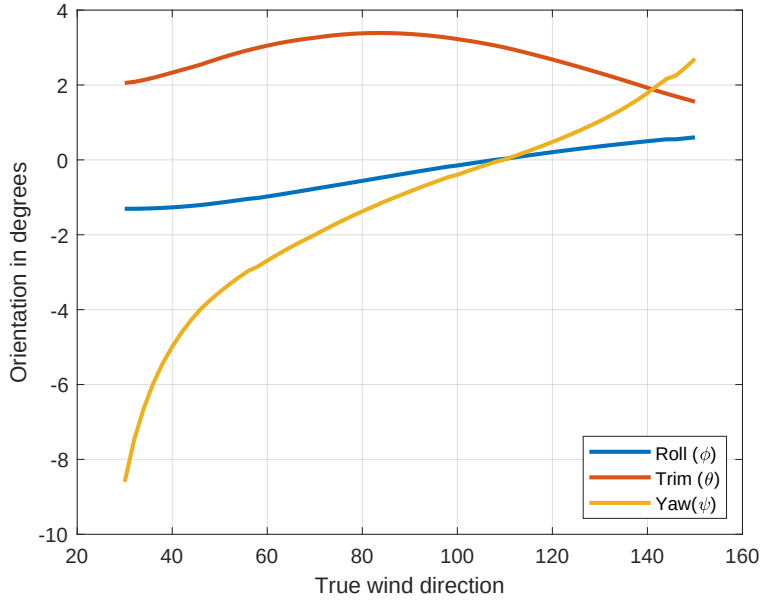

Figure B.4: Wind velocity: 12m/s

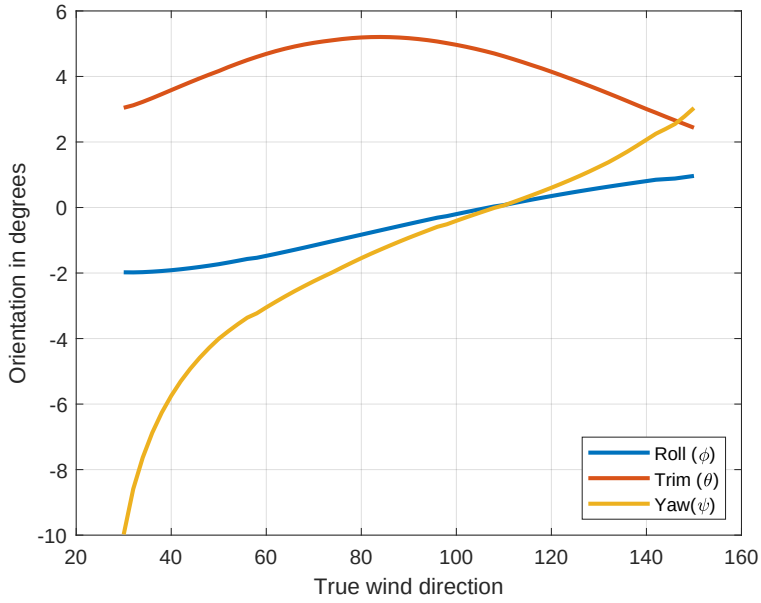

Figure B.5: Wind velocity: 15m/s

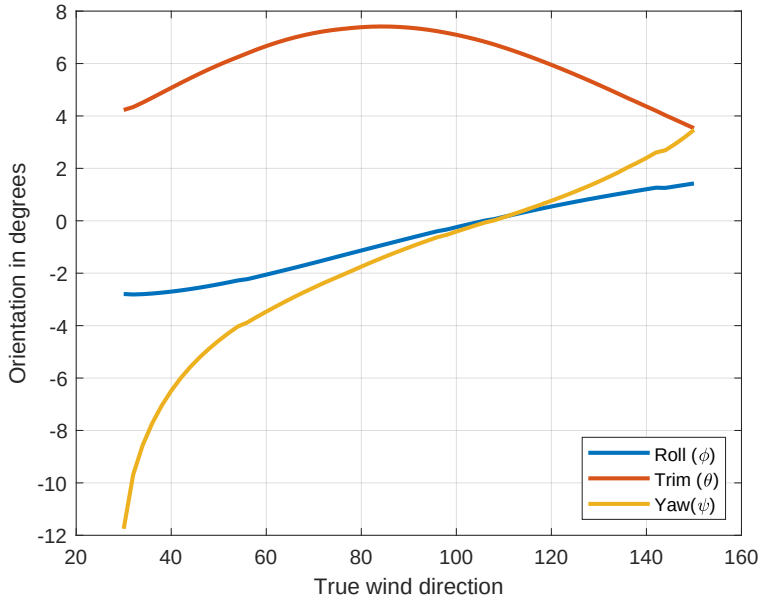

Figure B.6: Wind velocity: 18m/s

Appendix C

VPP resistance

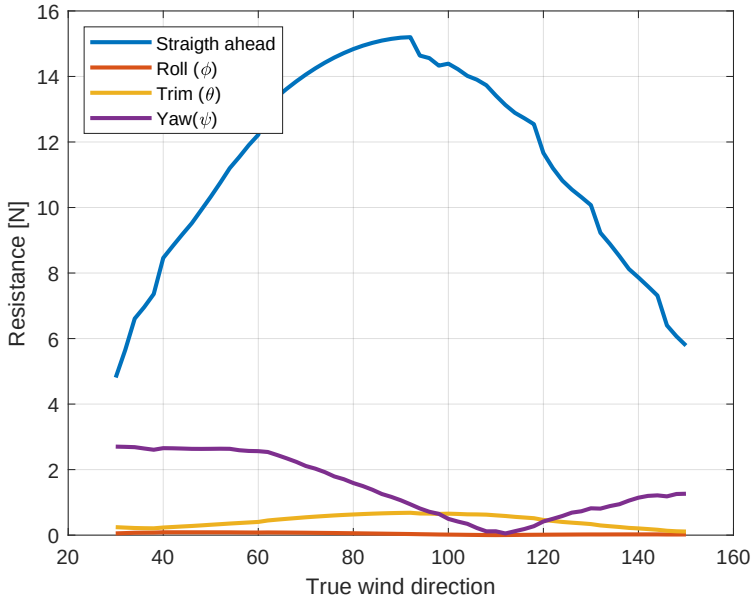

Figure C.1: Wind velocity: 3m/s

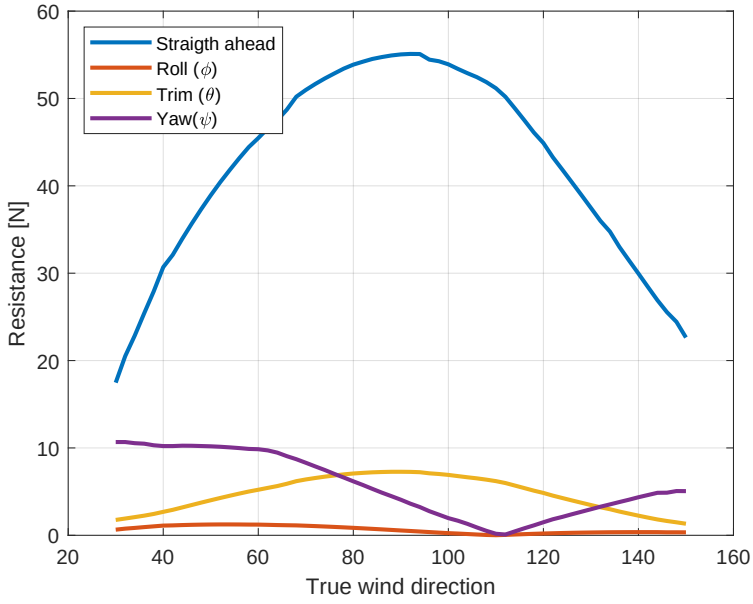

Figure C.2: Wind velocity: 6m/s

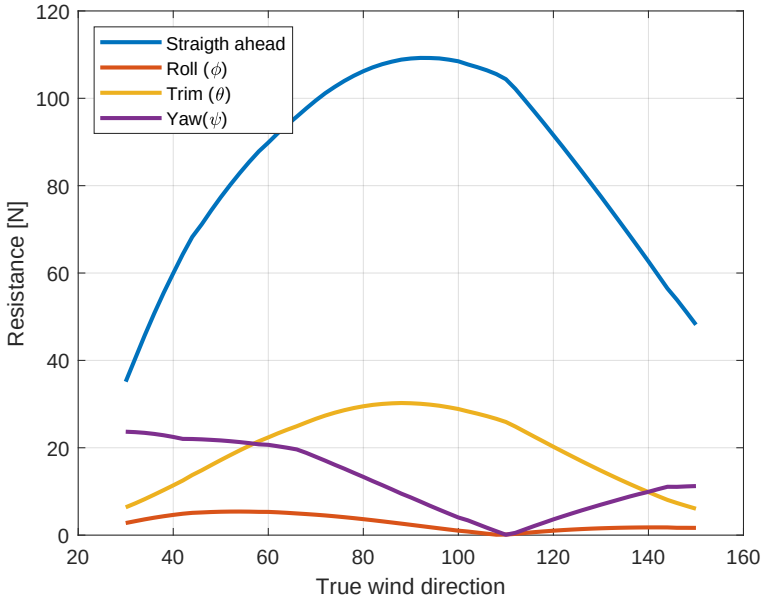

Figure C.3: Wind velocity: 9m/s

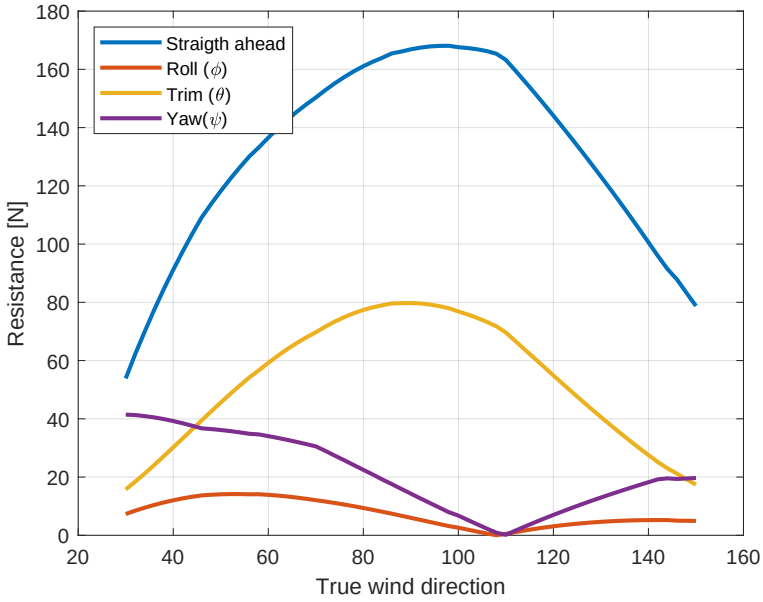

Figure C.4: Wind velocity: 12m/s

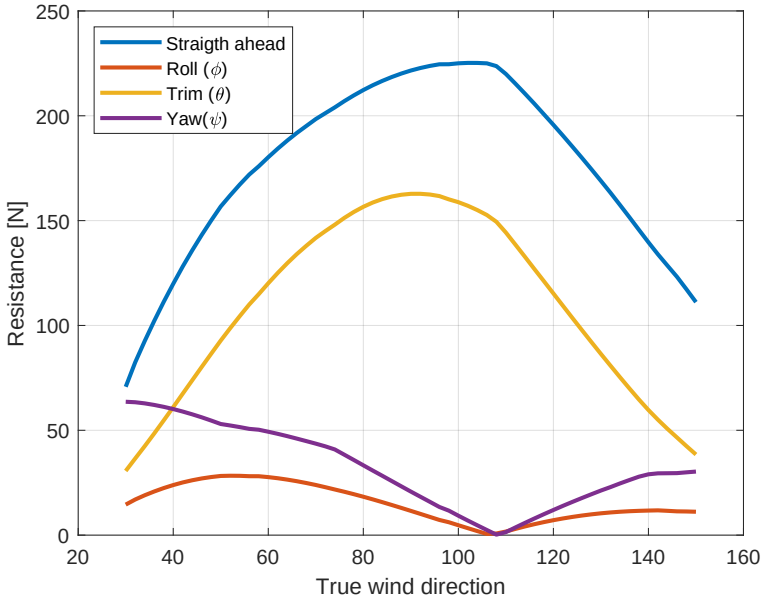

Figure C.5: Wind velocity: 15m/s

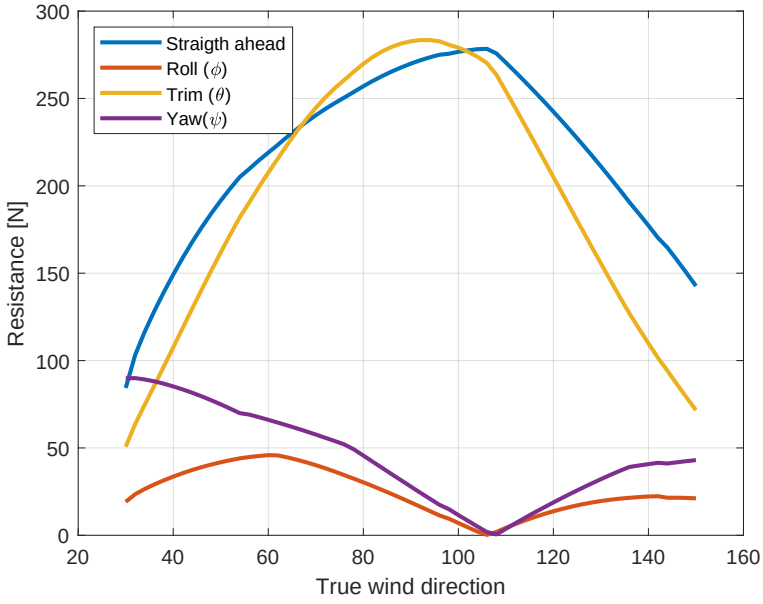

Figure C.6: Wind velocity: 18m/s